

TEL AVIV UNIVERSITY

Raymond and Beverly Sackler
Faculty of Exact Sciences
School of Physics & Astronomy



אוניברסיטת תל-אביב

הפקולטה למדעים מדויקים
ע"ש ריימונד וברלי סאקלר
בית הספר לפיסיקה ואסטרונומיה

Conformations of Polymers in Confined Spaces

Thesis submitted as part of the requirements for the degree of
Master of Science (M.Sc.) in Physics at Tel Aviv University
School of Physics and Astronomy

by

Nir Alfasi

The research work for this thesis was carried out
under the supervision of **Prof. Yacov Kantor**

August 2013

Acknowledgments

I wish to thank my supervisor, Professor Yacov Kantor, whose guidance, support and endless patience enabled me to study and understand the field of polymers, and complete this thesis. I also wish to thank Mr. Yosi Hammer for his insightful advice and guidance.

I could not have done this work without the support of my beloved wife. This work is dedicated to her.

Abstract

Recent progress in single molecule manipulation methods allows us to measure forces in the pN range. In these methods, a polymer is usually attached by one end to the tip of a microscopic probe, approaching a surface. The force is then measured with respect to the displacement of the probe. In this work, we investigate these polymer-mediated forces. In our model, the force is purely entropic, with amplitude \mathcal{A} which is determined by the difference between the universal exponent η of two different scale-invariant geometries.

We investigate these forces through the conformations of ideal polymers in such geometries. By finding the conformation of a polymer, we can find the end-to-end distance of the polymer, which is related to the exponent η . We use simulation of a diffusing particle on a lattice to derive η for several scale-invariant geometries, such as cones with various cross-sections, two circular cones and cone touching a plane. We only look at the limit of long polymers, while the surfaces are all considered infinite.

The results of our simulations match analytical predictions perfectly. We also investigate many geometries that cannot be studied analytically. We find that the more confined the polymer is, the larger the end-to-end distance is. We show that if the polymer is more confined at one area in space, it ‘escapes’ to the more open area in space and its properties change accordingly.

We also investigate the winding angle of a polymer connected to a cone near a plane. We find that short polymers do not surround the cone, but ‘escape’ to one side and propagate there. We also study the winding angle of a monomer inside the polymeric chain, and find no conclusive evidence that it changes when the polymer is elongated.

Contents

1	Introduction	1
1.1	Single Molecule Manipulation Methods	1
1.2	Polymer Size	3
1.3	The Ideal Chain	5
1.3.1	Lattice Random Walk Models	5
1.3.2	Off-Lattice Random Walk Models	8
2	Review of Relevant Results	10
2.1	Ideal Polymers Behavior Near an Impenetrable Wall	10
2.2	Ideal Polymers in Scale Invariant Geometries	11
2.3	Polymer-Mediated Forces	14
2.4	Winding Angles	16
3	Various Cones Configurations	18
3.1	Numerical Method	18
3.2	Ideal Polymer Inside a Circular Cone	20
3.2.1	Two Dimensional Case	20
3.2.2	Three Dimensional Case	23
3.3	Ideal Polymer Inside Cones with Various Cross Sections	25
3.4	Ideal Polymer Between Two Circular Cones	28
3.4.1	Two Coaxial Cones	28
3.4.2	Upright Cone and a Tilted Cone	29
3.4.3	Two Touching Cones	35
4	Cone-Plane Configurations	40
4.1	Ideal Polymer Between an Upright Cone and a Plane	40
4.2	Ideal Polymer Between a Tilted Cone and a Plane	41
4.2.1	Tilted Cone near a Plane	41
4.2.2	Cone Lying on a Plane	48
5	Winding Angle Distributions	50
5.1	Monte Carlo Simulation	50
5.2	Winding Angle Distributions of an Ideal Polymer Near a Circular Rod	51
5.3	Winding Angle Distributions of an Ideal Polymer Between a Cone and a Plane	53
6	Conclusions and Future Prospects	58
A	Simulation of Diffusing Particle on a Lattice	60
B	Numerical Monte Carlo Simulation	62
	References	66

Chapter 1

Introduction

In this work, we study the conformations of ideal polymers connected to impenetrable surfaces in various geometries. The reason for interest in such configuration is the recent progress in single molecule manipulation techniques, which allows us to measure the properties of a single macromolecule directly. All single molecule manipulation methods require a probe, which is usually of microscopic dimensions, that can generate or detect forces and displacements. In these experiments, a single macromolecule, such as polymer, is attached to the probe and held close to a surface and the force vs. displacement is measured.

This chapter reviews methods for the investigation of polymer's properties, as well as a brief introduction to polymer physics and a more thorough overview of the ideal chain model used in this work.

1.1 Single Molecule Manipulation Methods

Single molecule manipulation methods can be divided into two groups [1–3]. *Mechanical transducers* apply or sense forces through the displacement of a bendable beam. The most common examples for this type of method are scanning force microscopy (SFM) cantilevers (Fig. 1.1(a)), also known as atomic force microscopy (AFM), and microneedles (Fig.1.1(b)). The other group is the *external field manipulators*, where external fields act on the molecules from a distance. These fields can be used to exert forces on molecules by acting either on the molecules themselves or through other ‘handles’ attached to the molecule itself. In this group we can find optical tweezers (Fig. 1.1(c)) and magnetic tweezers (Fig. 1.1(d)).

Atomic force microscopy (AFM) has developed significantly in recent years, and is now considered one of the most accurate methods for single molecule manipulation. In this method, the polymer is attached at one end to a sharp tip (of the order of nanometers at the sharpest point) of a flexible force-sensing cantilever, where the other end can be either attached to a base or left loose. The tip can then be moved in the x , y or z direction, and the force F_{ts} exerted on the tip by the sample is measured through the deflection of the cantilever, using optical methods (interferometer, beam-bounce) or electrical methods (piezoresistive, piezoelectric) [4–6]. *Glass microneedles*

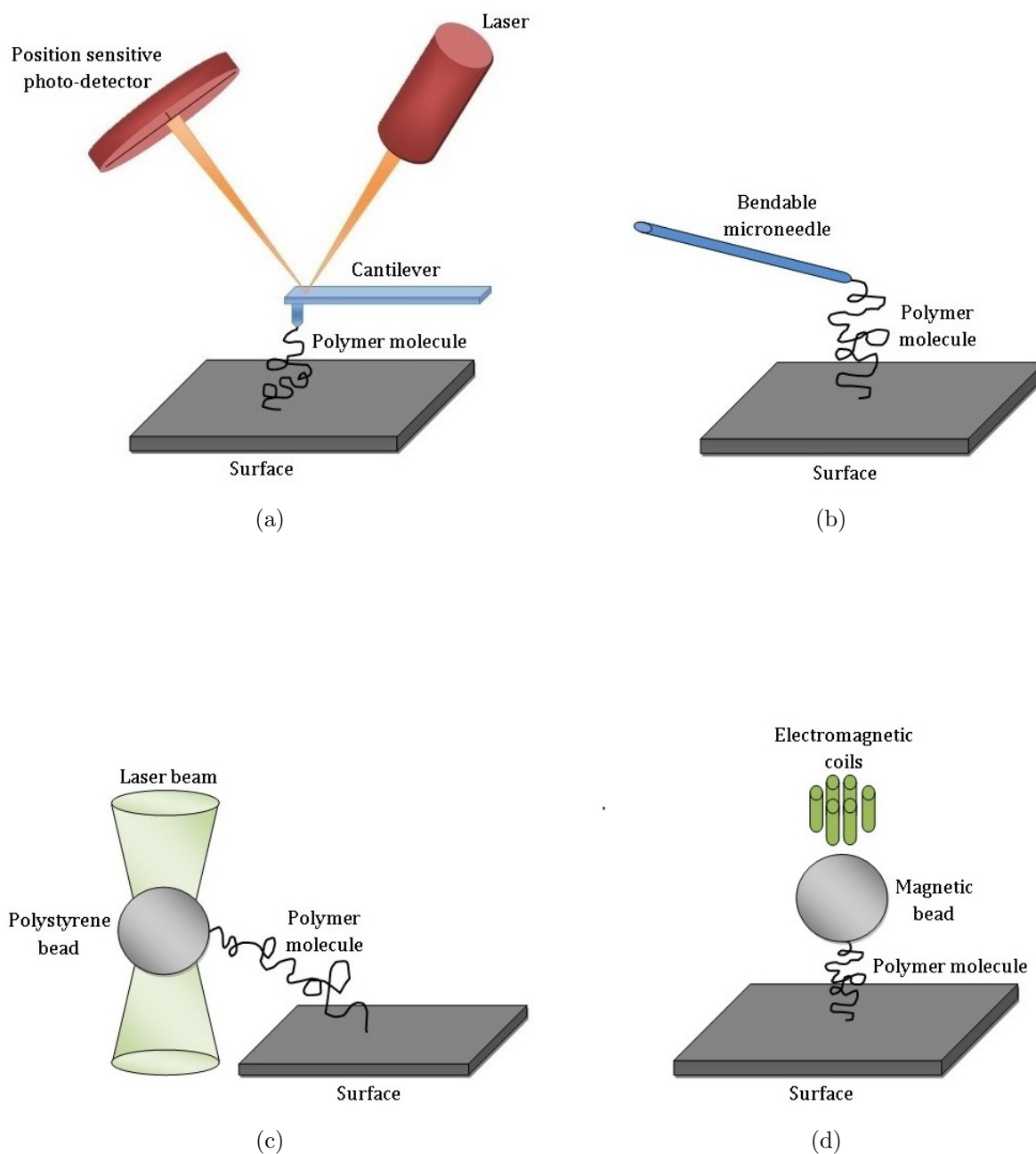


Figure 1.1: Single molecule manipulation methods: (a) atomic force microscopy, (b) bendable microneedle, (c) optical tweezers, (d) magnetic tweezers. Based on figures from [1–3]

are based on the same principle as the AFM [7]. The polymer is attached to the tip of a long and narrow glass tube (of the order of nanometers at the tip), as the needle moves and the force applied by the polymer on the needle is measured through the microneedle deflection.

External field manipulators only technically differ from the above methods, while their goal is similar. In *optical tweezers*, a near-infrared laser beam is tightly focused by a high numerical aperture microscope objective to create a large spatial gradient in light intensity [8]. When these gradient optical forces exceed those from scattering, an object is attracted to the point of highest intensity formed by focused light and can be stably trapped at this position in all three dimensions. The magnitude of these optical forces is generally insufficient to stably trap biological macromolecules themselves, but more than adequate for manipulating microscopic dielectric objects, such as micron-sized polystyrene beads, which are usually biochemically linked to the molecule or polymer of interest. Manipulation of the bead position is possible by changing the focus of the beam, while the other end of the polymer is usually attached to a fixed surface. The force applied by the polymer can then be determined by measuring the displacement of the bead from its equilibrium position [3]. *Magnetic tweezers* are similar to the optical tweezers, only that the force is applied on a micron-sized superparamagnetic bead via magnetic fields [9]. The molecule is stretched and coiled by positioning and rotation of an external magnet, respectively. The end-to-end distance of the molecule can be measured by extracting the x , y , and z positions of the bead using video microscopy [10].

All of the above methods give us the ability to measure forces in the pN range [1]. The application of force on the polymer allows us to extend it to its full length, measure its properties and compare it to its coiled free state, giving us experimental verification to the magnitude of global properties of a single polymer.

1.2 Polymer Size

A linear homopolymer¹, is a long flexible molecule composed of large number of small, simple and identical units, called monomers. The number of monomers N composing a polymer is called the degree of polymerization. In order to understand the properties of polymeric materials we must consider a large assembly of molecules.

¹From this point on, when writing polymer we mean homopolymer, as we will not discuss heteropolymers in this work. Further reading is available in [11].

However, for polymers, each molecule consists of a large number of units, so in order to investigate even a single molecule, we need to use statistical mechanics methods. Experimentally, investigation of the properties of a single polymer can be achieved by placing it in a dilute solution, so that interactions between the polymers can be neglected. This allows us to investigate a single polymer, while ignoring external effects.

Two main quantities are usually used to define the size of the polymer - *radius of gyration* and *end-to-end vector* [11]. In this work, we are interested in the conformation of a polymer - the spatial structure of the polymer, determined by the relative locations of its monomers. Since we are interested in the macro properties of the polymer, we use the end-to-end vector \vec{R} to describe the conformation of the polymer, as well as the winding angle of the polymer, which will be discussed later in this work. The end-to-end vector \vec{R} is defined as the vector connecting one end of the polymer to the other. By dividing a polymer with $N + 1$ monomers into N segments, we can define \vec{b}_n to be the vector of the n th bond (Fig. 1.2). The end-to-end vector can therefore be defined as:

$$\vec{R} \equiv \sum_{n=1}^N \vec{b}_n. \quad (1.1)$$

Since the distribution of \vec{R} is frequently isotropic, the average is $\langle \vec{R} \rangle = 0$. Therefore, in order to investigate the polymer's conformations and properties, we need to use the mean-square end-to-end distance:

$$\langle R^2 \rangle \equiv \sum_{i=1}^N \sum_{j=1}^N \langle \vec{b}_i \cdot \vec{b}_j \rangle. \quad (1.2)$$

We can therefore characterize the size of the polymer by $\sqrt{\langle R^2 \rangle}$.

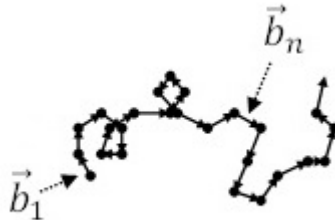


Figure 1.2: An ideal polymer subdivided into N segments. Each segment can be described as a vector \vec{b}_n .

There are many factors influencing the exact properties of a polymer, such as the degree of polymerization, type and size of the monomers, interactions between monomers and the type of solvent the polymer is dissolved in. The conformation that the polymer adopts, depends on three characteristics: flexibility of the chain, interactions between monomers on the chain and interactions with surroundings. We investigate the properties of a single, isolated polymer chain and neglect any interactions between the monomers themselves. A thorough review on polymer physics can be found in [11–13].

1.3 The Ideal Chain

In this work, we only consider the conformations of chains with no interactions between monomers along the chain, even if they overlap. Such chains are called *ideal chains*. This situation is obviously impossible for real polymers, but there are several types of polymeric systems with nearly ideal chains. Such a system for example, is a polymeric dilute solution in a solvent held in a special temperature, called the θ -temperature. While the ideal polymer is only theoretical, it has great significance to the study of polymers. It is relatively easy to investigate and it provides useful insights into more complicated models, in the same manner that ideal gas does not actually exist, while it is vastly used as a framework for more complex models.

1.3.1 Lattice Random Walk Models

The simplest way to describe an ideal polymer is by replacing it with random walk (RW) on a lattice [14–16], as shown in Fig. 1.3. Despite simplifications such as discretization, the RW model shares some global features with ideal polymers. In this model, a polymer with $N + 1$ monomers is replaced by a N steps random walk. Each step is made from one lattice site to one of its nearest neighbors, chosen randomly with equal probability $\frac{1}{z}$, where z is the lattice coordination number. We use hypercubic lattice, thus $z = 2d$, d being the space-dimension (in this work we use $d = 2$ or $d = 3$). For RW, steps i and j are independent for $i \neq j$, meaning $\langle \vec{b}_i \cdot \vec{b}_j \rangle = \langle \vec{b}_i \rangle \langle \vec{b}_j \rangle = 0$ for $i \neq j$. Therefore:

$$\langle R^2 \rangle = \sum_{i=1}^N \sum_{j=1}^N \langle \vec{b}_i \cdot \vec{b}_j \rangle = a^2 \sum_{i=1}^N \sum_{j=1}^N \delta_{ij} = Na^2, \quad (1.3)$$

equation (1.4) in terms of N and \vec{R} :

$$p\left(\vec{R} - \vec{a}_k, N - 1\right) = p\left(\vec{R}, N\right) - \frac{\partial p}{\partial N} - \sum_{\alpha} \frac{\partial p}{\partial R_{\alpha}} a_{k\alpha} + \sum_{\alpha, \beta} \frac{1}{2} \frac{\partial^2 p}{\partial R_{\alpha} \partial R_{\beta}} a_{k\alpha} a_{k\beta}, \quad (1.5)$$

where $a_{k\alpha}$ and R_{α} are the components of \vec{a}_k and \vec{R} respectively. Inserting (1.5) into (1.4), using the relations

$$\frac{1}{z} \sum_{k=1}^z a_{i\alpha} = 0, \quad (1.6)$$

$$\frac{1}{z} \sum_{k=1}^z a_{k\alpha} a_{k\beta} = \frac{\delta_{\alpha\beta} a^2}{d}, \quad (1.7)$$

yields:

$$\frac{\partial p}{\partial N} = \frac{a^2}{2d} \nabla^2 p \equiv D \Delta p, \quad (1.8)$$

which is the well known diffusion equation. In equation (1.8), N mimics the time t usually used in the diffusion equation, so each step is effectively equal to one time unit.

By solving equation (1.8) with certain initial and boundary conditions, we can find the probability density function² of the end point of the polymer $P(\vec{R}, N)$, for any geometry corresponding to the conditions used. For example, a random walker in d -dimensions starting from the origin with no boundary restrictions, which is equivalent to an ideal polymer pinned to a specific point at one end and free in the other end, corresponds to the initial condition $P(\vec{R}, N = 0) = \delta^d(\vec{R})$. By solving equation (1.8) with this condition, we can find the probability density for an ideal polymer in free space (denoted by “fs”):

$$P_{\text{fs}}\left(\vec{R}, N\right) = \left(\frac{d}{2\pi N a^2}\right)^{d/2} \exp\left(-\frac{dR^2}{2N a^2}\right). \quad (1.9)$$

It can be noted that $P_{\text{fs}}(\vec{R}, N)$ coincides with $\langle R \rangle = 0$ and the result in (1.3).

²From now on, when using the term probability distribution, we refer to the probability density function as defined here.

1.3.2 Off-Lattice Random Walk Models

Lattice models as discussed above impose many restrictions on the system, such as equal step size and orthogonal steps only. In order to generalize the problem, RW models can also be conducted off-lattice. In a simple off-lattice model called *freely jointed chain* [11], each step is still of length a , but the step can take any orientation in d -dimensions. Since \vec{b}_i and \vec{b}_j are still independent, equation (1.3) gives the same result, as well as other general relations described in the previous Section. There are many other off-lattice models describing the conformation of an ideal polymer. While each model adds a new constraint for the system, usually on the ‘short-range’ interactions, all of these models neglect ‘long-range’ interactions.

One known off-lattice model is the *Gaussian chain model* [13,17]. This model is widely used due its great mathematical simplicity. We assume that the bond vector \vec{b} itself follows a Gaussian distribution, meaning:

$$P(\vec{b}) = \left(\frac{d}{2\pi a^2}\right)^{d/2} \exp\left(-\frac{db^2}{2a^2}\right). \quad (1.10)$$

Let \vec{R}_n denote the position of the n th segment in the chain relative to the first segment, denoted by \vec{R}_0 (Fig. 1.4). The probability density of $\vec{b}_n = \vec{R}_n - \vec{R}_{n-1}$ is given by (1.10), while the probability distribution of the set $\{\vec{R}_n\} \equiv (\vec{R}_1, \dots, \vec{R}_N)$

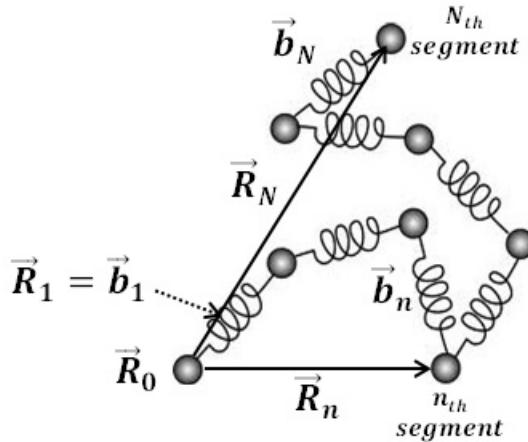


Figure 1.4: The Gaussian chain described using beads and springs. The positions of the segments relative to the first bead are denoted by \vec{R}_n , while the connecting vectors are marked by \vec{b}_n .

is given by:

$$P\left(\{\vec{R}_n\}\right) = \left(\frac{d}{2\pi a^2}\right)^{dN/2} \exp\left(-\frac{d}{2a^2} \sum_{n=1}^N \left(\vec{R}_n - \vec{R}_{n-1}\right)^2\right). \quad (1.11)$$

Consider a series of ‘beads’ connected by harmonic springs of natural length 0 with spring constant k (as seen in Fig. 1.4). The energy of such chain can be written as

$$U = \frac{1}{2}k \sum_{n=1}^N \left(\vec{R}_n - \vec{R}_{n-1}\right)^2. \quad (1.12)$$

Using the Boltzmann distribution $P \propto \exp(-U/k_B T)$ to describe the equilibrium state of such system, by choosing the spring constant to be

$$k = \frac{dk_B T}{a^2}, \quad (1.13)$$

the equilibrium distribution of the chain is exactly as described in equation (1.11). Therefore, we have introduced an analogous model to describe an ideal polymer using energy, where the probability density of such model follows the Gaussian density function, thus simplify calculations.

Chapter 2

Review of Relevant Results

In this chapter we review some known results in the field of our research. We look at properties such as end-to-end distance, force and winding angle of an ideal polymer near an impenetrable wall and other scale-invariant geometries, setting the basis for our work.

2.1 Ideal Polymers Behavior Near an Impenetrable Wall

As seen in Section 1.3, the probability density function of the end point of an ideal polymer $P(\vec{R}, N)$ can be found using the diffusion equation (1.8). Consider an ideal polymer in d -dimensions near an impenetrable wall at $x_1 = 0$. This is the case of an ideal polymer near a *repulsive* boundary at $x_1 = 0$, while in the language of RW and diffusion, the exclusion of paths that cross the boundaries is accomplished by assuming that these are *absorbing* surfaces. The starting position of the polymer is denoted by \vec{r}^i and its end point by \vec{r}^f . We can find $P_{\text{hs}}(\vec{R}, N)$ (“hs” denotes half-space) using the method of images [14, 18], as seen in Fig. 2.1 for the two-dimensional case. The solution is simply the difference between the solution of an ideal polymer in free space (Eq. (1.9)) starting at $\vec{r}^i = (x'_1, x'_2, \dots, x'_d)$ and the solution of a RW starting at $\vec{r}^i = (-x'_1, x'_2, \dots, x'_d)$. For $N \gg 1$, we can approximate:

$$\begin{aligned} P_{\text{hs}}(\vec{r}^f, \vec{r}^i, N) &= P_{\text{fs}}(\vec{r}^f - \vec{r}^i, N) - P_{\text{fs}}(\vec{r}^f - \vec{r}^i, N) = \\ &= \left(\frac{d}{2\pi Na^2}\right)^{d/2} \left(\exp\left\{-\frac{d(\vec{r}^f - \vec{r}^i)^2}{2Na^2}\right\} - \exp\left\{-\frac{d(\vec{r}^f - \vec{r}^i)^2}{2Na^2}\right\} \right) = \\ &= \left(\frac{d}{2\pi Na^2}\right)^{d/2} \exp\left\{-\frac{d(\vec{r}^f - \vec{r}^i)^2}{2Na^2}\right\} \left[1 - \exp\left\{-\frac{2dx_1 x'_1}{Na^2}\right\}\right] \simeq \\ &\simeq Cx_1 \exp\left\{-\frac{dR^2}{2Na^2}\right\}, \end{aligned} \tag{2.1}$$

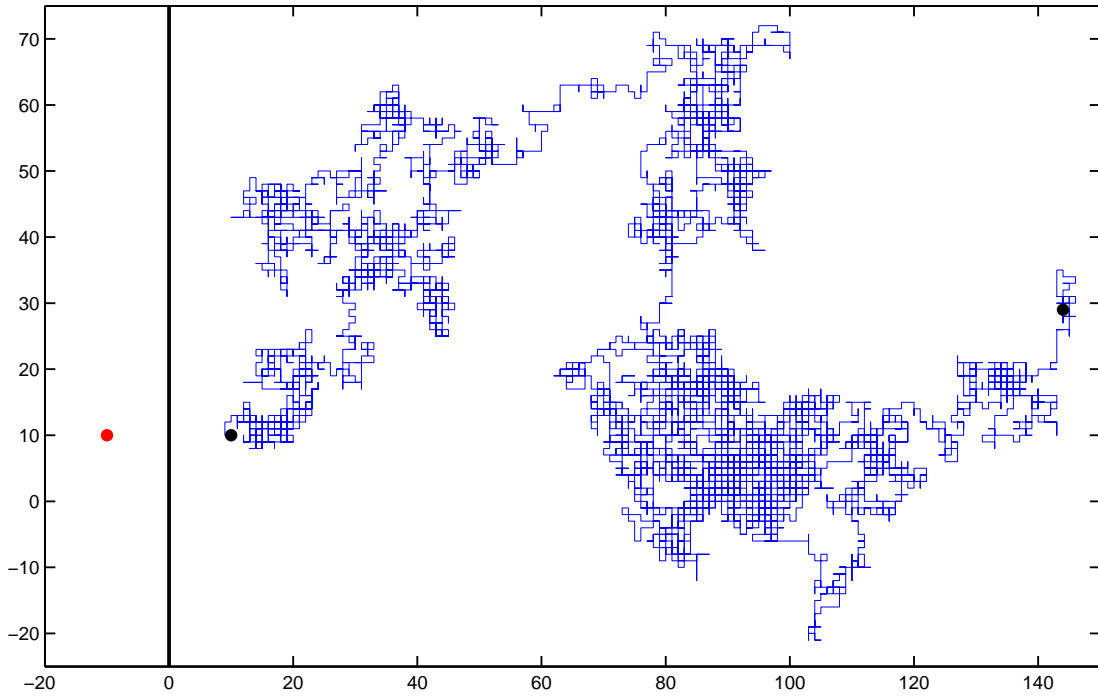


Figure 2.1: Random walk in 2D confined to the half space defined by $x > 0$. The black dots mark the start point $\vec{r}' = (10, 10)$ and end point \vec{r} . The red dot indicates the mirror image at $\vec{r}'' = (-10, 10)$.

where C is a constant with dimensions of $(\text{length})^{-d}$ and we assumed that the polymer size is much larger than the distance of the initial point from the origin, i.e. $\frac{r'}{\sqrt{Na^2}} \ll 1$. From $P_{\text{hs}}(\vec{R}, N)$, we can find $\langle R^2 \rangle_{\text{hs}}$ under the above condition:

$$\langle R^2 \rangle_{\text{hs}} \simeq Na^2 \left(1 + \frac{1}{d} \right). \quad (2.2)$$

2.2 Ideal Polymers in Scale Invariant Geometries

Solving the problem of ideal polymer near a wall using the method of images was possible since the boundary conditions allowed us to use this method. We now present a different method for solving this problem, that will not be confined only to geometries where the method of images is applicable, but to more general configurations.

Looking at the results found so far, we notice that N and a always show up in the form Na^2 . It can be shown, that all polymer properties are invariant under the transformation $a \rightarrow \frac{a}{\sqrt{\lambda}}$ and $N \rightarrow \lambda N$ [17]. This means that if there is no other length scale in the problem other than a , the mean square end-to-end distance will

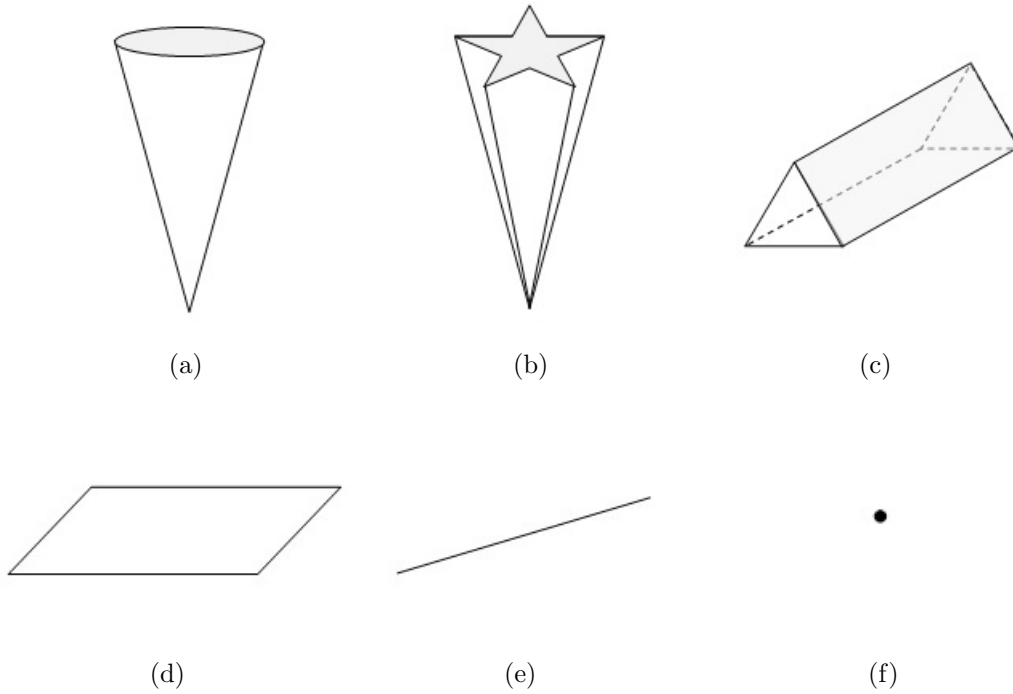


Figure 2.2: Examples for three-dimensional figures without length scale: (a) circular cone, (b) star-shaped cone, (c) three-dimensional wedge, (d) infinite plane, (e) a line and (f) a dot. All figures are infinite, where the gray surface indicates truncation for graphic purposes. The polymer can be attached to the tip of a surface at one end, while the other end is either free or attached to another probe.

follow the rule:

$$\langle R^2 \rangle = \text{const} \cdot N a^2. \quad (2.3)$$

In order for the above relation to apply when the polymer is situated in a certain geometry, the geometry should have no length scale. Such geometries are called *scale-invariant geometries*. Examples for such geometries are depicted in Fig. 2.2.

We look at an ideal polymer in scale-invariant geometry, starting from \vec{r}' and ending at point \vec{r} . Since \vec{r}' adds a length scale to the problem, we must consider long polymers $N \gg 1$, meaning $r' \ll r$, so we can consider the end-to-end vector to be equal to the end point of the polymer $\vec{R} \simeq \vec{r}$. Our goal is to find a general solution $P(\vec{R}, N)$ to the diffusion equation (1.8) in scale-invariant geometries, and use it to investigate the conformations of ideal polymers. This solution does not have to satisfy the initial condition $P(\vec{R}, N = 0) = \delta^d(\vec{R})$, since we are looking at $N \gg 1$.

Consider the Laplacian in spherical coordinates in d -dimensions:

$$\Delta P = \frac{1}{R^{d-1}} \cdot \frac{\partial}{\partial R} \left(R^{d-1} \frac{\partial P}{\partial R} \right) + \frac{1}{R^2} \Delta_{S^{d-1}} P, \quad (2.4)$$

where $\Delta_{S^{d-1}}$ is the Laplace-Beltrami operator on the $d - 1$ unit sphere, known also as the spherical Laplacian [19]. Note that the separation between the angular dependence and the radial dependence is a general property of this operator, and is valid for any configuration. For the case of a polymer in scale-invariant geometry, we can assume separation between the radial part and the angular part of $P(\vec{R}, N)$:

$$P(R, \theta_i, N) = f(R, N) \cdot g(\theta_i), \quad (2.5)$$

where θ_i denote the $d - 1$ angular coordinates of the end point, with $i = 1, \dots, d - 1$. Note that we look at the limit of:

$$\frac{r'}{\sqrt{DN}} \ll 1 \simeq \frac{r}{\sqrt{DN}}, \quad (2.6)$$

and therefore we neglect the dependence in the start point of the polymer. In the form of (2.5), we consider the following ansatz:

$$P(R, \theta_i, N) = A (DN)^\alpha R^\eta \exp \left\{ -\frac{R^2}{4DN} \right\} g(\theta_i), \quad (2.7)$$

where A is a constant with dimensions of $(\text{length})^{-(\eta+2\alpha+d)}$. Inserting (2.7) into the diffusion equation in (1.8), using the Laplacian property in (2.4) and the following relations:

$$\nabla^2 P = \left[\frac{\eta(d-2) + \eta^2}{R^2} - \frac{(\eta + \frac{d}{2})}{DN} + \frac{R^2}{4D^2N^2} \right] P, \quad (2.8)$$

$$\frac{\partial P}{\partial N} = \left[\frac{\alpha}{N} + \frac{R^2}{4DN^2} \right] P, \quad (2.9)$$

yields:

$$\left[\frac{R^2}{DN} \left(\alpha + \eta + \frac{d}{2} \right) - \eta(\eta - d - 2) \right] \cdot g(\theta_i) = \Delta_{S^{d-1}} g(\theta_i). \quad (2.10)$$

The problem is now reduced to an eigenvalues equation. We must demand the above

relation to hold for every R , leading to

$$\alpha + \eta + \frac{d}{2} = 0 \quad \Rightarrow \quad \alpha = - \left(\eta + \frac{d}{2} \right). \quad (2.11)$$

The eigenvalues equation thus reduces to

$$\Delta_{S^{d-1}} g = -\eta(\eta - d - 2) g, \quad (2.12)$$

where η is the only exponent missing in the probability density function described in (2.7). Since $g(\theta_i)$ is part of the probability density, we must demand that $g(\theta_i) > 0$ for every θ_i within the boundary conditions. Therefore, we must always choose the lowest eigenvalue in (2.12) as the exponent η [20]. Since we find η by solving (2.12) using the appropriate boundary conditions, it follows that η is determined only by the angular equation and the angular boundary conditions.

As stated before, our goal in this work is to investigate polymer conformations using $\langle R^2 \rangle$. From $P(\vec{R}, N)$ it follows:

$$\langle R^2 \rangle = 2DN(\eta + d). \quad (2.13)$$

The relation in (2.13) is of great importance for this work. This relation means that $\langle R^2 \rangle$ is determined by 3 factors - the number of monomers N , the diffusion coefficient D and most importantly the exponent η . By finding $\langle R^2 \rangle$, we can find the exponent η and consequently the radial part of $P(\vec{R}, N)$. For example, by comparing $P_{\text{hs}}(\vec{R}, N)$ from (2.1) to the general form in (2.7) we can see that $\eta = 1$ for half-space configuration. By inserting this value into (2.13) and using $D = \frac{a^2}{2d}$, we get:

$$\langle R^2 \rangle_{\text{hs}} = 2 \left(\frac{a^2}{2d} \right) N(1 + d) = Na^2 \left(1 + \frac{1}{d} \right), \quad (2.14)$$

exactly as found earlier in (2.2).

2.3 Polymer-Mediated Forces

Consider an ideal polymer attached to the tip of a solid circular cone approaching a solid infinite plane. This setup is used in some single molecule manipulation methods discussed in Section 1.1, such as the atomic force microscopy. In this setup, the only

length scale is provided by the tip-plate separation h (Fig. 2.3(a)), since we assume $a \ll h \ll R$. Neglecting any structure associated with the polymer, variations in free energy when the cone approaches the plane are purely entropic, i.e. due to the change in the number of conformations the polymer can take. The change in free energy \mathcal{F} is therefore proportional to $k_B T$. Since force has dimensions of energy divided by length and h is the only length scale in the problem, the entropic force must be written as [21]:

$$F = \mathcal{A} \frac{k_B T}{h}, \quad (2.15)$$

where \mathcal{A} is a dimensionless geometry-dependent pre-factor.

From equation (2.7), we can find the total number of possible conformations the polymer can take, by integrating over all spatial coordinates:

$$\mathcal{N}_s \propto z^N N^{-\eta_s/2}, \quad (2.16)$$

where the subscript “s” is used to describe the geometry we use. For example, “s=hs” for half-space (used before), “s=c” for cone (Fig. 2.3(b)) and “s=cp” for cone-plate configuration¹ (Fig. 2.3(c)).

The change in free energy when bringing the cone with the polymer attached to its tip (Fig. 2.3(b)) to contact the plane (Fig. 2.3(c)) is due to the change in entropy:

$$\Delta \mathcal{F} = -T \Delta S = T (S_c - S_{cp}) = \frac{1}{2} k_B T (\eta_c - \eta_{cp}) \ln N, \quad (2.17)$$

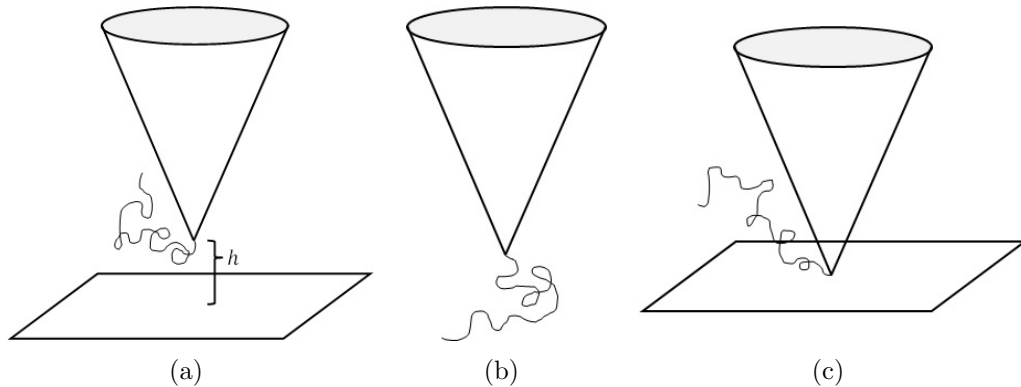


Figure 2.3: An ideal polymer attached to the tip of a solid circular cone (a) in distance h from a solid plane, (b) very far from the plane and (c) touching the plane.

¹We shall henceforth use a subscript to describe the geometry when discussing η , $P(\vec{R}, N)$ and \mathcal{N} . When we discuss these measures in general, we will not use any subscript.

where the entropy $S = k_B \ln \mathcal{N}$ is calculated using (2.16). $\Delta \mathcal{F}$ is equal to the work done against the entropic force. Since for $h \gtrsim R$ we consider the cone to be far enough from the plate, the change in the free energy only occurs for $a \leq h \leq R$:

$$\Delta \mathcal{F} = W = \int_R^a \mathcal{A} \frac{k_B T}{h} dh = -\mathcal{A} k_B T \ln \left(\frac{R}{a} \right) \simeq -\frac{1}{2} \mathcal{A} k_B T \ln N, \quad (2.18)$$

where we have considered only the leading term for $N \gg 1$. Equating (2.17) and (2.18), using a more general notation of η_{initial} and η_{final} for any two configurations (instead of cone and cone-plate), leads to the relation:

$$\mathcal{A} = (\eta_{\text{final}} - \eta_{\text{initial}}). \quad (2.19)$$

This implies that the amplitude of the force mediated by the polymer and acting on a surface in a non-scale-invariant geometry, is the difference between two exponents describing scale-invariant geometries. Therefore, we simply need to find $\langle R^2 \rangle$ for ideal polymers in two scale-invariant geometries, use relation (2.13) to deduce η and find the polymer mediated-force acting on the plane. For example, as can be seen in (1.9), in free space $\eta_{\text{fs}} = 0$, where in half-space $\eta_{\text{hs}} = 1$, as seen in (2.1). Thus, if we look at a polymer pinned at one end to a point in distance h from a plane, the pre-factor in (2.15) is simply $\mathcal{A} = 1$.

2.4 Winding Angles

So far we have only discussed the end-to-end vector as a tool for studying the conformations of polymers, though it gives us information only about the position of the end point of the polymer, without any knowledge of its detailed conformation. While the positions of all the polymer monomers can be found easily, their exact location gives us too much unnecessary information. A measure that can give us more knowledge about its true state, especially when placed near impenetrable surfaces, is the *winding angle distribution*.

A two-dimensional random walker starting in the vicinity of a point or finite object, tends to follow a path which will eventually wrap around that object [22]. We want to investigate the wrapping of a polymer around a circular cone, when the polymer is attached to the tip of the cone touching an impenetrable plane, as depicted in Fig. 2.4(a). The winding angle Θ of a polymer is defined as the angle

that is swept out by the polymer, as can be seen in Fig. 2.4(b) for a two-dimensional polymer around a circle.

Since for ideal polymers there is no preferred direction, it follows that $\langle \Theta \rangle = 0$. Therefore, we will be interested in the root-mean-square of the winding angle $\sqrt{\langle \Theta^2 \rangle}$. This measure indicates how many times the polymer is wrapped around the cone, with respect to the degree of polymerization N .

Rudnick and Hu [22] showed linear dependence between $\sqrt{\langle \Theta^2 \rangle}$ and $\ln N$ for ideal polymer near a two-dimensional circle (Fig. 2.4(b)) and near a three-dimensional rod (Fig. 2.4(c)):

$$\sqrt{\langle \Theta^2 \rangle} = a_0 \ln N + b_0. \quad (2.20)$$

They showed that $a_0 = \frac{1}{\sqrt{12}} \simeq 0.289$ for any d and is independent of the radius of the circle or rod. A more thorough review on winding angles and winding angles distributions can be found in [23, 24].

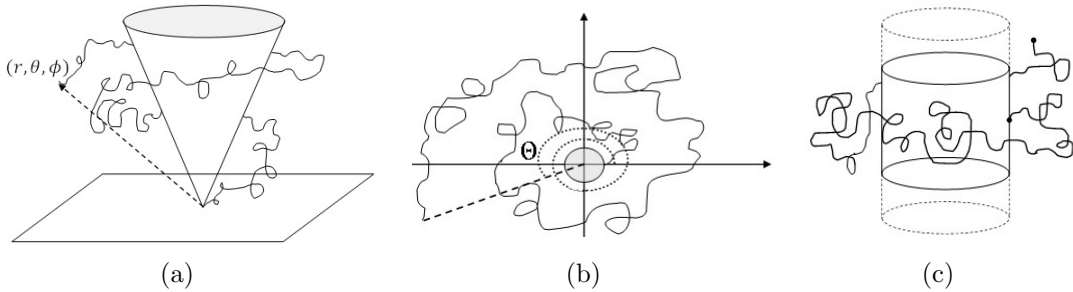


Figure 2.4: (a) An ideal polymer attached to the tip of a circular cone touching an impenetrable plane. The polymer in this sketch is wrapped around the cone. The winding angle Θ cannot be drawn, but it obviously satisfies $\Theta > 2\pi$, and differs from the polar angle θ . (b) An ideal polymer around an excluded circular area (in gray). The winding angle Θ is the angle between the starting direction of the polymer, which is analogous to the first step of a random walker, and the end point of the polymer (dotted line). (c) An ideal polymer wrapped around a circular rod. The winding angle Θ cannot be shown here.

Chapter 3

Various Cones Configurations

In this chapter we present results for ideal polymers attached to the tip of a cone with various cross sections and in several geometries. We start by describing the numerical method used in this work. We then look at an ideal polymer inside a wedge in two dimensions and inside a circular cone in three dimensions. For these two configurations we can find $P(\vec{R}, N)$ analytically, and compare it to numerical results. These cases will help us verify our numerical simulations. We present numerical values of η for a polymer inside cones with square and star cross-sections and a polymer between two circular cones in several configurations.

3.1 Numerical Method

As discussed earlier, the statistical mechanics of an ideal polymer near an impenetrable surface is equivalent to that of a RW or a diffusing particle near an absorbing boundary. Therefore, we can either create many random walks on a lattice in order to acquire the statistics of the problem or we can solve the problem of a discrete diffusion of a particle once, and use the probability density of the end of the polymer $P(\vec{R}, N)$ to study macroscopic properties. We will use the second method, since it is easier to implement, it requires less computational resources and it gives us $P(\vec{R}, N)$ directly. Since for an absorbing boundary condition, the tip of the cone is a forbidden site, the starting point of the diffuser cannot be exactly at the tip of the cone. We place it at distance $r' = a$ from the tip of the cone, where a is the lattice constant. For long walks, this will be negligible compared to the macroscopic length scale we are looking at, satisfying $\frac{r'}{\sqrt{DN}} \ll 1$.

We solve the diffusion equation (1.8) with the initial condition

$$P(\vec{R}, N = 0) = \delta_{ra} \delta_{\theta 0} \delta_{\phi 0}. \quad (3.1)$$

In each time step there is equal probability of $\frac{1}{2d}$ for moving to each of the neighboring sites, where forbidden sites has 0 probability. We let the diffusion continue for time N , where at the end of the diffusion we get $P(\vec{R}, N)$. Calculation of the mean-square

end-to-end vector $\langle R^2 \rangle$ is done by summation over all lattice sites:

$$\langle R^2 \rangle = \frac{\sum_{\text{All lattice sites}} r_i^2 \cdot p_i}{\sum_{\text{All lattice sites}} p_i}, \quad (3.2)$$

where r_i is the radial distance from the initial point to the site i and p_i is the probability for locating the end of the polymer at that site. Note that due to the boundary conditions $\sum_i p_i < 1$.

Since the diffusion is done on a lattice, the discretization causes malformation of the surface. Since all of our geometries have no length scale, by looking at $N \rightarrow \infty$ we can eliminate this bias. We find $P(\vec{R}, N)$ in equal intervals of N and calculate $\langle R^2 \rangle$ as a function of N . As seen before, $\langle R^2 \rangle$ is proportional to Na^2 for large N :

$$\lim_{N \rightarrow \infty} \frac{\langle R^2 \rangle}{Na^2} = c_0, \quad (3.3)$$

where c_0 is a dimensionless constant. Since $r' = a$, and we are looking at the limit of

$$\frac{r'}{\sqrt{DN}} = \frac{\sqrt{2da}}{a\sqrt{N}} \sim \frac{1}{\sqrt{N}} \ll 1. \quad (3.4)$$

It follows that

$$\frac{\langle R^2 \rangle}{Na^2} = c_0 + c_1 \left(\frac{1}{\sqrt{N}} \right) + c_2 \left(\frac{1}{\sqrt{N}} \right)^2 + \dots, \quad (3.5)$$

where the c_i s are dimensionless constants. Therefore, from (3.5) and (2.13) it follows:

$$\eta(N) = d \left[c_0 - 1 + c_1 \left(\frac{1}{\sqrt{N}} \right) + c_2 \left(\frac{1}{\sqrt{N}} \right)^2 + \dots \right]. \quad (3.6)$$

We are interested in the large N limit, so we finally get:

$$\eta \equiv \lim_{N \rightarrow \infty} \eta(N) = d(c_0 - 1). \quad (3.7)$$

A more thorough description about the numerical method and its errors can be found in Appendix A.

3.2 Ideal Polymer Inside a Circular Cone

3.2.1 Two Dimensional Case

In the two-dimensional case, we are looking at an ideal polymer inside an excluded wedge with opening angle α , as depicted in Fig. 3.1(a). The polymer is attached to the tip of the wedge at one end, while the other end is free. Note that $0 < \alpha < \pi$, where $\alpha = \pi/2$ denotes half space and $\alpha > \pi/2$ effectively denotes a polymer outside the wedge. This case has been solved analytically by Considine and Redner [25], where they found $P(\vec{r}, \vec{r}', N)$ to be:

$$\begin{aligned}
 P(\vec{r}, \vec{r}', N) &= \\
 &= \left(\frac{1}{\alpha DN} \right) \exp \left(\frac{-(r^2 + r'^2)}{4DN} \right) \sum_{\nu_n} \cos(\nu_n \theta) \cos(\nu_n \theta') I_{\nu_n} \left(\frac{rr'}{2DN} \right), \quad (3.8)
 \end{aligned}$$

where (r', θ') denote the starting point of the polymer and I_{ν_n} is the modified Bessel function. ν_n is a set of parameters depending on the wedge opening angle α , determined by satisfying the boundary condition:

$$\cos(\nu_n \alpha) = 0, \quad (3.9)$$

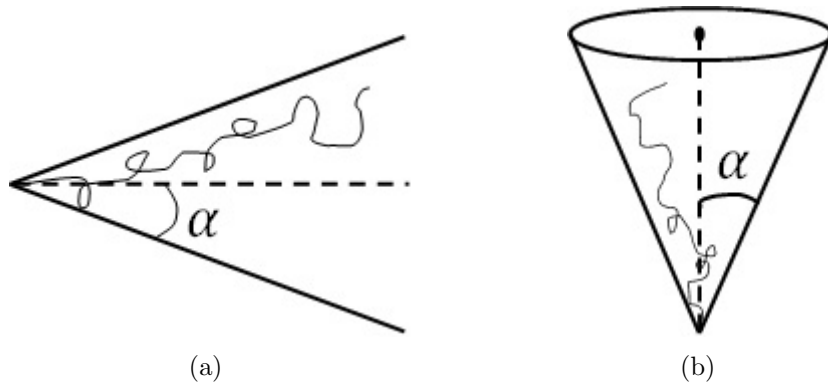


Figure 3.1: An ideal polymer inside (a) a two-dimensional wedge with opening angle α and (b) a three-dimensional circular cone with opening angle α . The case of $\alpha = \pi/2$ is a polymer in half-space, which we solved analytically in Section 2.1. Note that for $\alpha > \pi/2$, the polymer is actually ‘outside’ the wedge or cone.

meaning:

$$\nu_n = \frac{\pi}{2\alpha} (2n + 1) \quad , \quad n = 0, 1, 2, \dots \quad (3.10)$$

Since we are interested in the case of long polymers:

$$\frac{r'}{\sqrt{DN}} \ll 1 \simeq \frac{r}{\sqrt{DN}}, \quad (3.11)$$

we can use $I_\nu(x)$ power series expansion for small argument $x \ll 1$, and consider only the smallest term in the expansion [26]:

$$I_{\nu_n}(x) \simeq \frac{1}{\Gamma(\nu_n + 1)} \left(\frac{x}{2}\right)^{\nu_n}. \quad (3.12)$$

From (3.12), it can be seen that the smallest term is obtained for lowest ν_n , or $n = 0$ in Eq. (3.10). $P(\vec{r}, \vec{r}', N)$ therefore reduces to:

$$P(\vec{R}, N) \simeq A \left(\frac{R}{\sqrt{4DN}}\right)^{\nu_0} \exp\left\{-\frac{R^2}{4DN}\right\} \cos(\nu_0\theta), \quad (3.13)$$

where A is a constant with dimensions $(\text{length})^{-2}$, determined by α , r' , N and D .

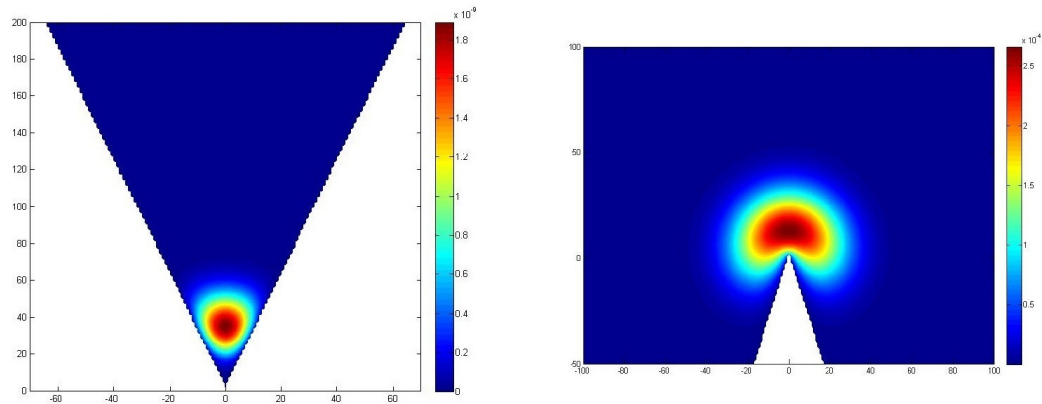
Comparing the above distribution to the general distribution described in equation (2.7), we can see that it is exactly the same for $d = 2$, where in this case $g(\theta) = \cos(\nu_0\theta)$. We can therefore conclude that the exponent η_w (“w” denotes wedge) is simply ν_0 , meaning:

$$\eta_w = \frac{\pi}{2\alpha}. \quad (3.14)$$

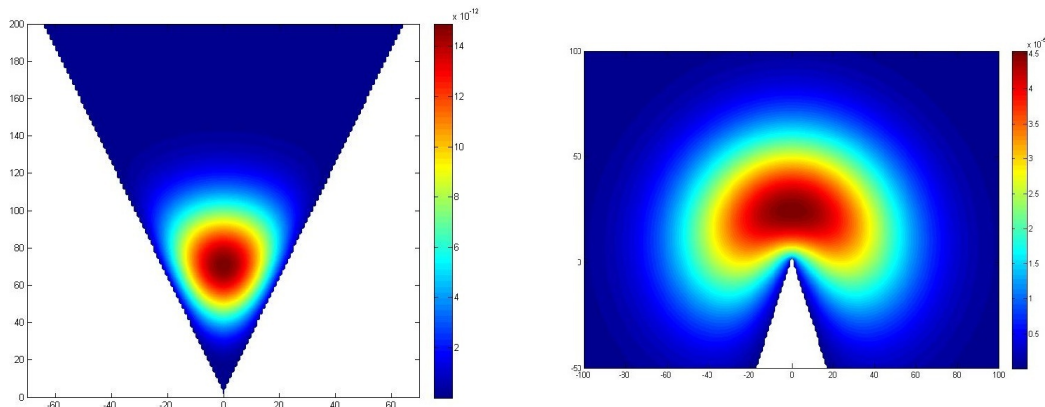
For example, for $\alpha = \pi/2$ (half-space), $\eta_{\text{hs}} = 1$, as found in Section 2.2.

Figs. 3.2 and 3.3 show $P(\vec{R}, N)$ for different polymer lengths inside and outside a wedge with $\alpha = \pi/10$. It can be seen that although the solution is evolving in time (Fig. 3.2), rescaling of the figures leads to the exact same form of the solution (Fig. 3.3). However, the wedge becomes smoother as we increase diffusion time. We can see that for $N = 500$ (Fig. 3.3(a)), the wedge has a serrated shape due to the discretization of the lattice, while For larger times, the discretization becomes more and more negligible and the wedge becomes ‘smoother’.

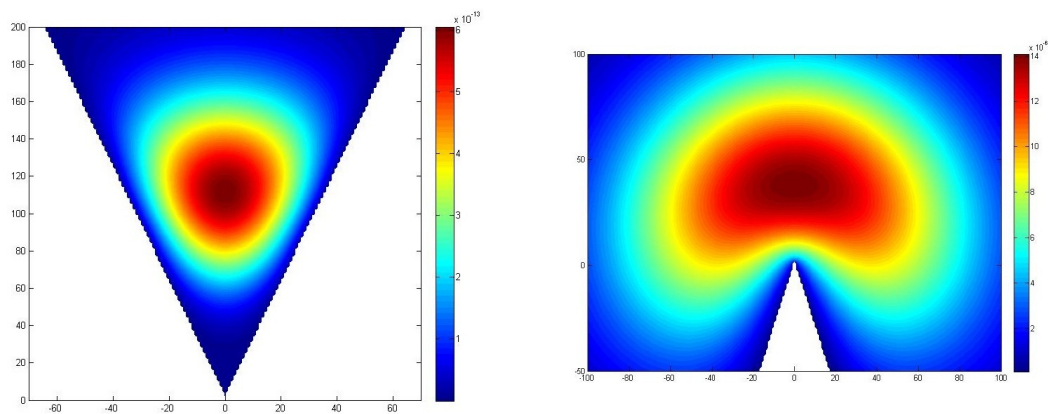
Fig. 3.5 shows comparison between numerical and analytical (from Eq. (3.14)) values of η_w as function of α , with excellent correspondence.



(a) $N = 500$.



(b) $N = 2000$.



(c) $N = 5000$.

Figure 3.2: $P(\vec{R}, N)$ for an ideal polymer attached to the tip of a two-dimensional wedge with $\alpha = \pi/10$. In the left column the polymer is inside the wedge, and outside in the right column. Images show three different polymer lengths: (a) $N = 500$ (b) $N = 2000$ (c) $N = 5000$.

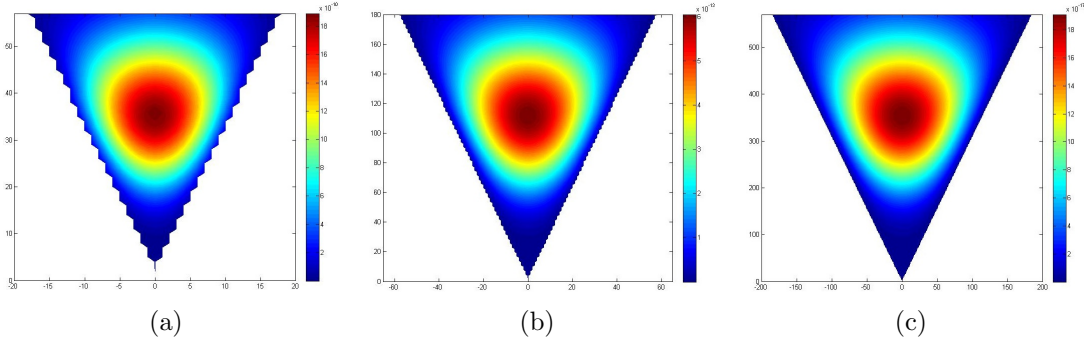


Figure 3.3: $P(\vec{R}, N)$ for an ideal polymer attached to the tip of a two-dimensional wedge with $\alpha = \pi/10$ for (a) $N = 500$, (b) $N = 5000$ and (c) $N = 50000$. These 3 figures emphasize the self similarity of the solution and the scale-invariance of the geometry. By rescaling, the shape of the probability density looks exactly the same in all times, while the shape of the cone becomes smoother as N grows.

3.2.2 Three Dimensional Case

We look at an ideal polymer inside a circular conical surface with opening angle α , as depicted in Fig. 3.1(b). For $\alpha > \pi/2$, the polymer is outside a circular cone with opening angle $\pi/2 - \alpha$, but we are still considering it to be ‘inside’ the cone. The probability density function of the end point of the polymer was found by Carslaw and Jaeger [18]:

$$P(\vec{r}, \vec{r}', N) = -\frac{1}{4\pi DN\sqrt{rr'}} \exp\left(-\frac{r^2 + r'^2}{4DN}\right) \times \sum_{\nu} \left[I_{\nu+1/2}\left(\frac{rr'}{2DN}\right) (2\nu+1) \sum_{m=0}^{\infty} \left(\frac{\epsilon_m P_{\nu}^{-m}(\mu) P_{\nu}^{-m}(\mu') \cos(m(\phi - \phi'))}{(1-\mu_0)^2 \frac{\partial}{\partial \mu} P_{\nu}^{-m}(\mu_0) \frac{\partial}{\partial \nu} P_{\nu}^{-m}(\mu_0)} \right) \right], \quad (3.15)$$

where P_{ν}^{-m} is the associated Legendre function and we have used the notations $\mu \equiv \cos\theta$, $\mu_0 \equiv \cos\alpha$ and $\mu' \equiv \cos\theta'$. In order for the above function to satisfy boundary conditions, the summation should be over all ν satisfying the condition [18]:

$$P_{\nu}^{-m}(\mu_0) = 0 \quad , \quad \nu > -\frac{1}{2}. \quad (3.16)$$

As done in the two-dimensional case, we consider only the lowest order term in the sum. Thus, the exponent η_c (“c” denotes cone) is simply the lowest ν :

$$\eta_c = \min_{\nu} \left(\nu > -\frac{1}{2} : P_{\nu}(\cos\alpha) = 0 \right), \quad (3.17)$$

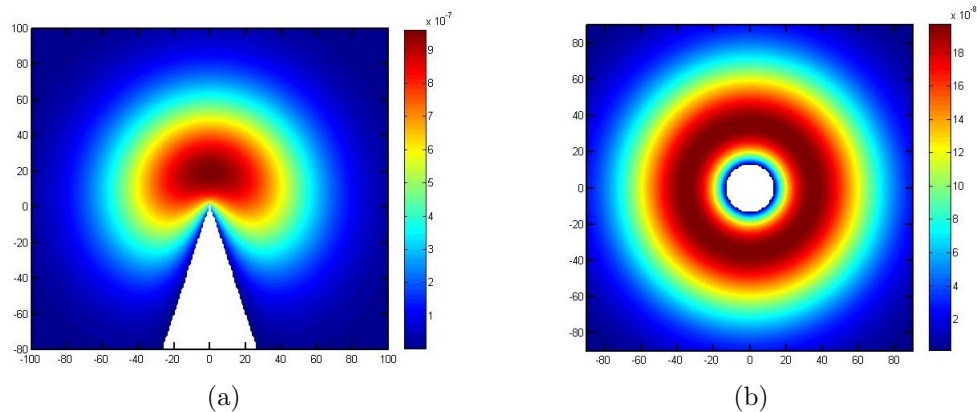


Figure 3.4: Cross sections of $P(\vec{R}, N)$ for an ideal polymer outside a circular cone with $\alpha = \pi/10$. Image in (a) shows vertical cross section of the density on the $x - z$ plane for $N = 4000$. Image in (b) shows transverse cross section of the density on $z = -40$ plane for $N = 4000$.

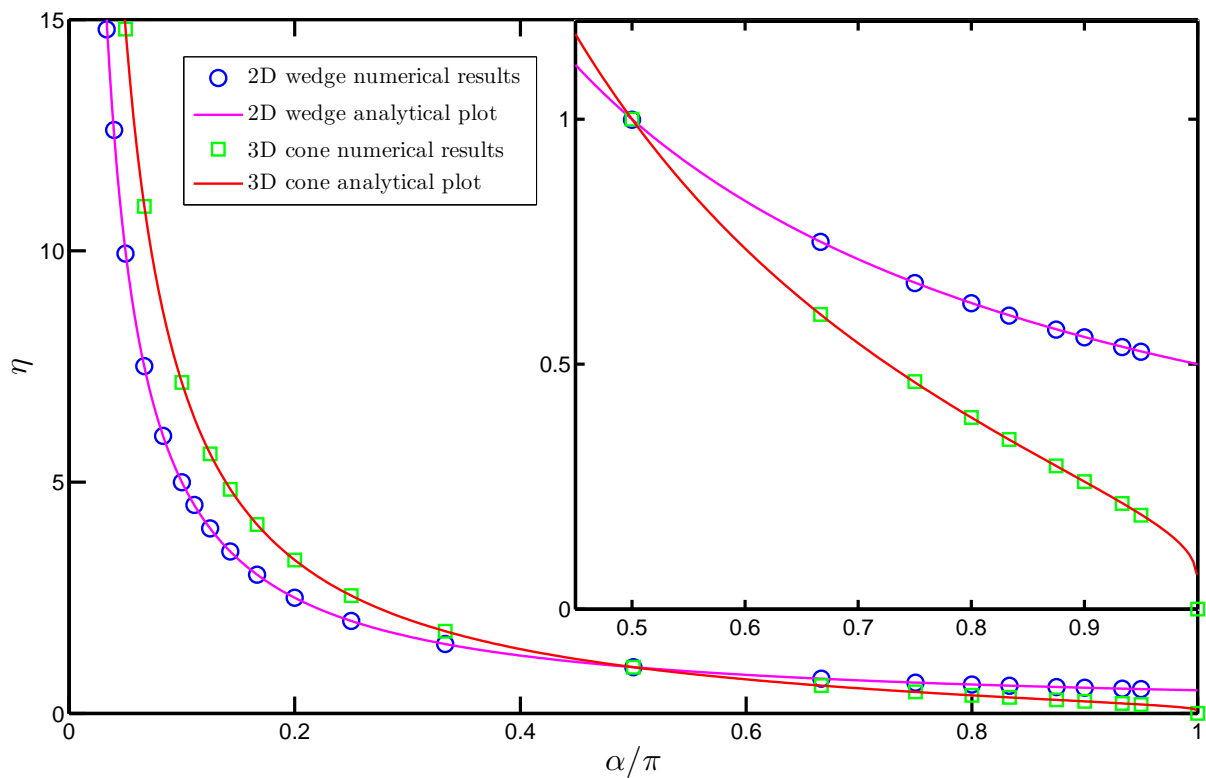


Figure 3.5: Plots of η as function of α for an ideal polymer inside a two-dimensional wedge (Fig. 3.1(a)) and a three-dimensional circular cone (Fig. 3.1(b)). Data points represent numerical results in 2D (blue circles) and 3D (green squares), while curves represent analytical plots in 2D (solid purple line) and 3D (solid red line). Error bars are too small to be shown.

where the initial condition was chosen to be $P(\vec{r}, \vec{r}', N) = \delta_{rr'} \delta_{\theta\theta_0} \delta_{\phi\phi_0}$ [25]. The lowest ν satisfying $P_\nu(\cos \alpha) = 0$ can be found numerically, and is considered as the analytical value.

Fig. 3.4 shows vertical and transverse cross sections of $P(\vec{R}, N)$ outside a circular cone with $\alpha = \pi/10$. It can be seen that the vertical cross section is identical to the probability density seen in the two-dimensional case (Fig. 3.2(c)). The transverse cross section shows that $P(\vec{R}, N)$ has azimuthal symmetry. Fig. 3.5 shows numerical and analytical (from Eq. (3.17)) values of η_c as function of α . It can be seen that the numerical values match perfectly to the analytical line. The two plots in Fig. 3.5 validate our numerical simulations, and give us confidence about the accuracy of our numerical results.

An interesting feature can be seen by looking at the values of η for $\alpha \rightarrow \pi$. While in three dimensions, the value of η_c goes to 0, meaning $\eta_c(\alpha = \pi) = \eta_{fs}$, in two dimensions this is not the case, as

$$\eta_w(\alpha = \pi) = 1/2. \tag{3.18}$$

This implies that a semi-infinite line changes the conformation of a polymer in two dimensions, but not in three dimensions. It appears that the polymer is ‘unaware’ of the presence of the ‘needle’, and therefore its conformation is the same as that of an ideal polymer in free space. This property is true for any $d \geq 3$.

3.3 Ideal Polymer Inside Cones with Various Cross Sections

In the previous section we have studied a polymer inside a circular cone in three dimensions, where we could find $P(\vec{R}, N)$ analytically. However, our simulations allow us to study conformations of polymers inside more ‘exotic’ cone shapes, where we cannot find $P(\vec{R}, N)$ analytically. While there is a variety of scale-invariant cone shapes, we choose to study cones with square and star cross sections, as described in Fig. 3.6, along with the circular cone from earlier.

Fig. 3.7 shows transverse cross sections of $P(\vec{R}, N)$ for the three cones studied. The affect of the discretization of the lattice can be seen, especially in the star-shaped cone. Although the serrated shape of the cone affects the value of $\eta(N)$, it should

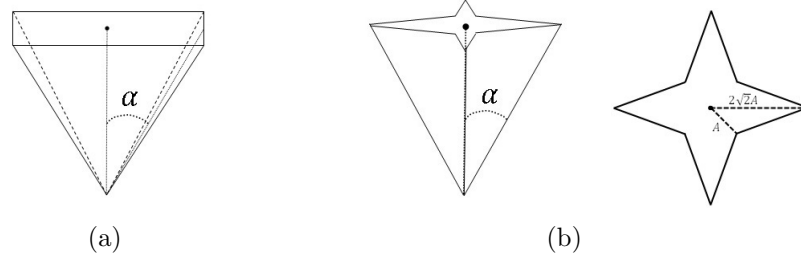


Figure 3.6: (a) Definition of opening angle α for cone with square cross section. α is defined as the angle between the apex of the cone and the center of the square side. (b) Definition of opening angle α for cone with four-pointed star cross section. α is defined as the angle between the apex of the cone and the star point. The inner angle γ is defined by the relation $\frac{\tan \gamma}{\tan \alpha} = 2\sqrt{2}$, as seen in the horizontal cross section.

have no effect on the value of η . Since our simulations are not truly infinite, it can be deduced that the smaller the cross-section of the shape is, more steps are needed in order to reach accurate numerical values of η .

Fig. 3.8 shows numerical values of η as function of α for several cones. It can be seen that η grows as the cross section of the cone becomes smaller. This implies that $\langle R^2 \rangle$ grows as the polymer is more confined. This property is independent of the cone shape, and is true for every geometry. Interesting feature can be seen in Fig. 3.7(c), as $P(\vec{R}, N)$ inside the star-shaped cone resembles that of a polymer inside a square-shaped cone rotated by 45° . The values of η in both cases are similar, yet not identical. This implies that while the polymer ‘prefers’ to stay in the center of the star-shaped cone, it also ‘travels’ inside the wings of the star. This extra space the polymer can enter, results in smaller $\langle R^2 \rangle$, and consequently in lower values of η .

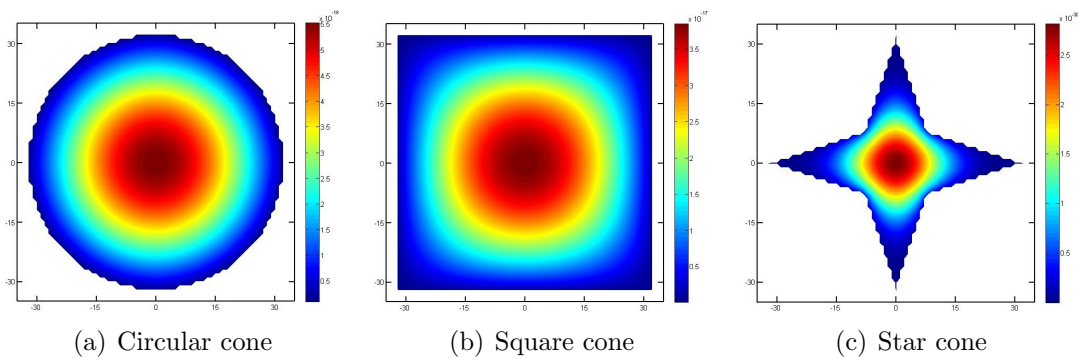


Figure 3.7: Transverse cross sections of $P(\vec{R}, N)$ for an ideal polymer inside (a) a circular cone, (b) a square-shaped cone and (c) a star-shaped cone. All cross sections show the $z = 100$ plane for $N = 4000$ and $\alpha = \pi/10$.

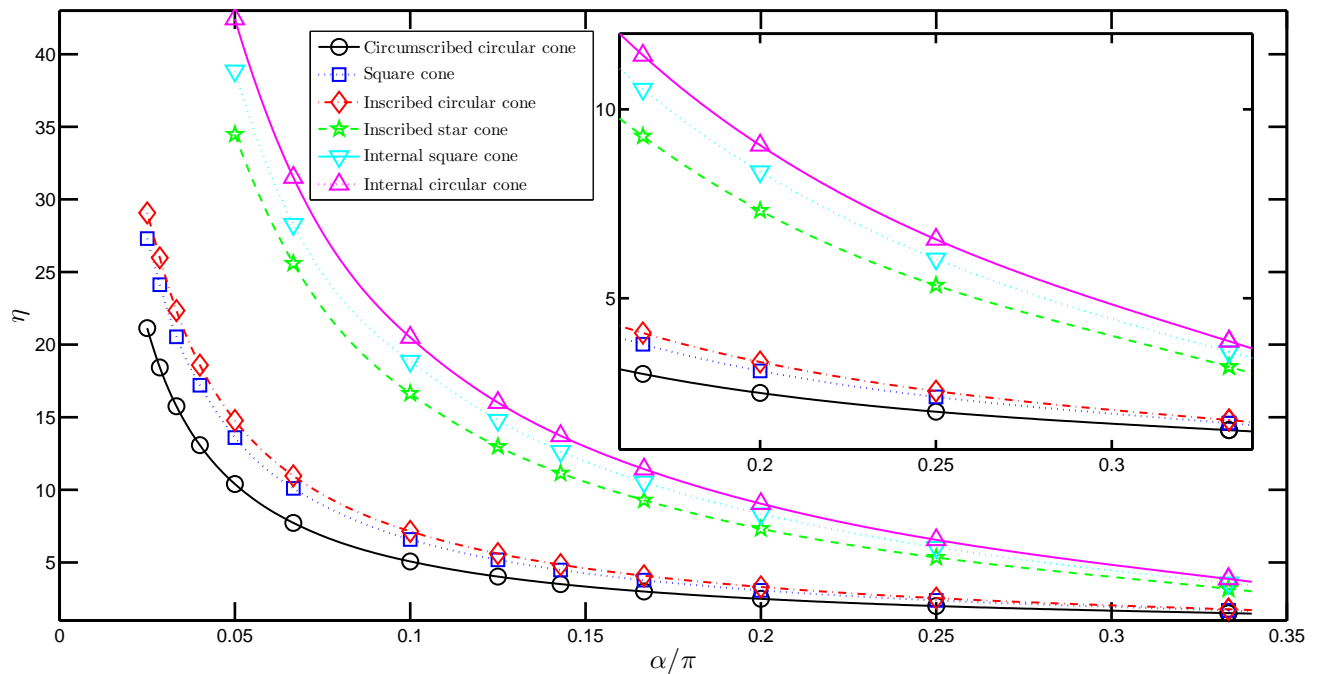
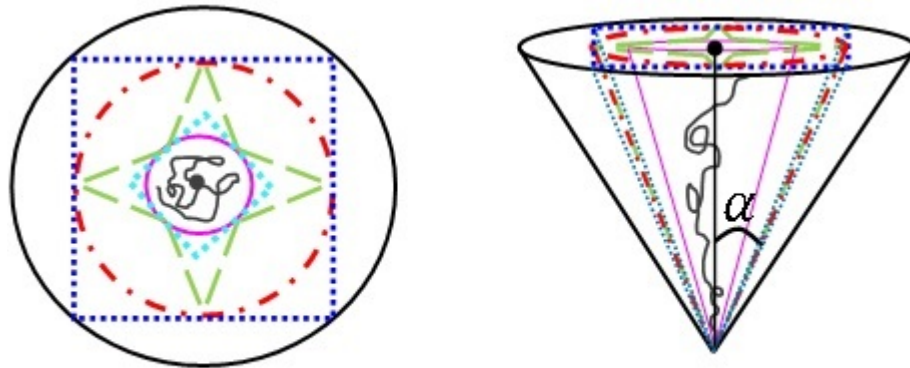


Figure 3.8: Numerical values of η as function of α for six cones according to the notation in the above sketches: circumscribed circular cone (black circles), square cone (blue squares), inscribed circular cone (red diamonds), star-shaped cone (green stars), internal square cone (cyan inverted triangles) and internal circular cone (purple triangles). The lines are simply interpolations of the points and are plotted only for convenience. Error bars are too small to be shown.

3.4 Ideal Polymer Between Two Circular Cones

3.4.1 Two Coaxial Cones

We look at the case of an ideal polymer between two circular cones with opening angles α_1 and α_2 , as depicted in Fig. 3.9(a). In order to find η analytically, we need to find the angular function $g(\theta, \phi)$ in (2.7) and solve equation (2.10) for $d = 3$:

$$\frac{1}{\sin \theta} \frac{\partial}{\partial \theta} \left(\sin \theta \frac{\partial g}{\partial \theta} \right) + \eta(\eta + 1) g = 0, \quad (3.19)$$

where ϕ dependence is absent due to azimuthal symmetry. In terms of $\mu \equiv \cos \theta$, (3.19) becomes [21]:

$$(1 - \mu^2) \frac{d^2 g}{d\mu^2} - 2\mu \frac{dg}{d\mu} + \eta(\eta + 1) g = 0. \quad (3.20)$$

The general solution for this equation is given by linear combination of the regular Legendre functions:

$$g(\theta) = a_1 P_\eta(\mu) + a_2 Q_\eta(\mu). \quad (3.21)$$

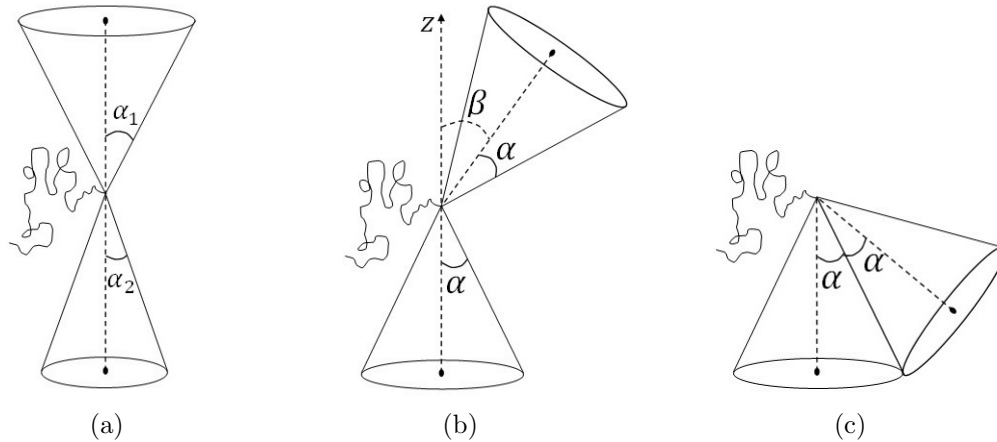


Figure 3.9: The three configurations studied in this section. (a) Two coaxial circular cones with opening angles α_1 and α_2 (denoted by “cc”). (b) Two circular cones with the same opening angle α , where the top cone is tilted by angle β with respect to the bottom cone’s axis (denoted by “tcc”). (c) Two touching circular cones (particular case of (b) for $\beta = \pi - 2\alpha$, denoted by “lc”).

For our geometry, we need to solve (3.20) under boundary conditions

$$g(\alpha_1) = g(\pi - \alpha_2) = 0. \quad (3.22)$$

The vanishing of g on the first cone gives rise to the relation:

$$\frac{a_2}{a_1} = -\frac{P_\eta(\cos \alpha_1)}{Q_\eta(\cos \alpha_1)}. \quad (3.23)$$

Imposing the vanishing of g on the second cone yields:

$$P_\eta(-\cos \alpha_2) Q_\eta(\cos \alpha_1) - Q_\eta(-\cos \alpha_2) P_\eta(\cos \alpha_1) = 0. \quad (3.24)$$

As done for the case of a single cone, we are interested in the smallest η solving the above equation, denoting it by η_{cc} (“cc” for cone-cone). The values of η_{cc} satisfying the above equation cannot be written as simple functions, but we can extract them numerically. These values will be referred to as the analytical values of η_{cc} .

We look at the case of $\alpha_1 = \alpha_2 \equiv \alpha$ (Fig. 3.9(a)). Vertical cross section of $P(\vec{R}, N)$ (Fig. 3.10) shows its azimuthal symmetry. Fig. 3.11 shows comparison between numerical and analytical values of η_{cc} as function of α , demonstrating the accuracy of our numerical simulations. This figure also shows comparison between η_{cc} and η_c for single cone from previous section. From this figure we see that for small α :

$$\eta_{cc}(\alpha, \alpha) \approx 2\eta_c(\alpha), \quad (3.25)$$

which is a particular case of:

$$\eta_{cc}(\alpha_1, \alpha_2) \approx \eta_c(\alpha_1) + \eta_c(\alpha_2). \quad (3.26)$$

This relation is true for small α_1 and α_2 [21] and the discrepancy increases with growing angles.

3.4.2 Upright Cone and a Tilted Cone

We now consider two circular cones in the configuration depicted in Fig. 3.9(b). In this configuration, azimuthal symmetry is lost and therefore $P(\vec{R}, N)$ cannot be found analytically. The distance between the cones is $2a$, where one end of the polymer is held in distance a from each tip. Since $\frac{a}{\sqrt{DN}} \ll 1$, the polymer can be

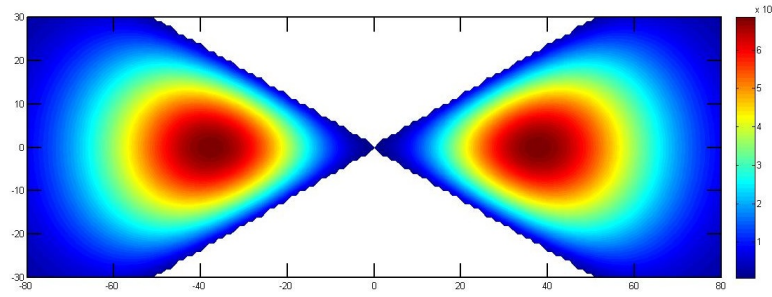


Figure 3.10: Vertical cross section of $P(\vec{R}, N)$ on the $x - z$ plane, for an ideal polymer with $N = 2000$ between two circular cones with $\alpha = \pi/3$.

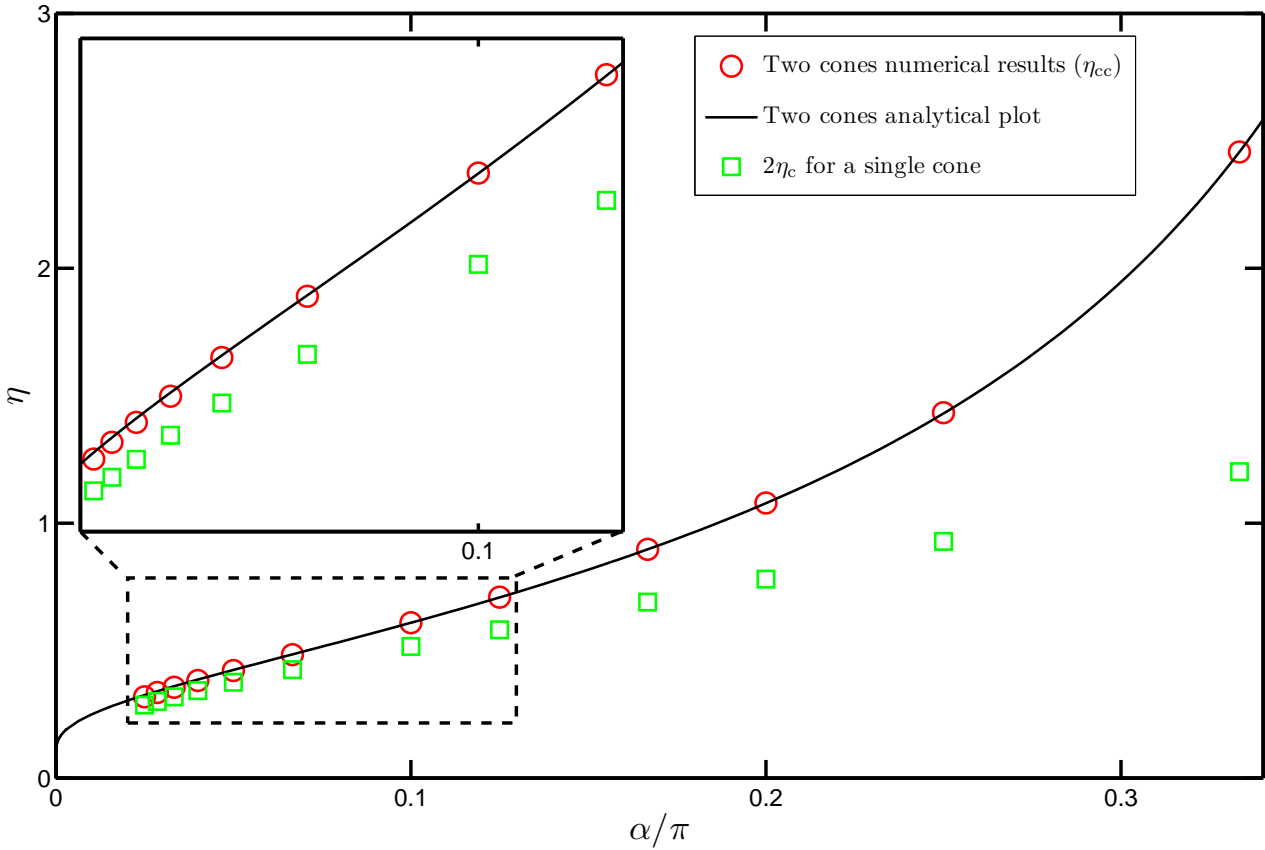


Figure 3.11: Plot of η as function of α for two cones configuration (Fig. 3.9(a)). The red circles show numerical values of η_{cc} , while the black solid line indicates the analytical values from equation (3.24). Green squares show $2\eta_c$, where η_c is taken from numerical simulations of a polymer outside a cone with opening angle α , as found in Section 3.2.2. Error bars are too small to be shown.

considered as attached to the two tips. We find numerically the dependence of η_{tcc} (“tcc” for tilted cone-cone) in β for $\alpha = \pi/5$, $\alpha = \pi/10$ and $\alpha = \pi/20$, as shown in Figs. 3.12, 3.14 and 3.16 respectively. The case $\beta = 0$ is that of two coaxial cones discussed earlier, while $\beta = \pi - 2\alpha$ will be discussed in the next section.

The results in the figures can be approximated by:

$$\eta_{tcc}(\beta) = a_0 + a_1 \exp \left\{ -a_2 \left(\frac{\beta}{\pi} \right)^2 \right\}, \quad (3.27)$$

where a_0 , a_1 and a_2 are fitting parameters. The fitting curves are shown by solid lines in Figs. 3.12, 3.14 and 3.16. Coefficients a_i are shown in Table 3.1. From this table and the corresponding figures, it can be seen that the Gaussian function used is suitable for the set of numerical values, as χ_{red}^2 shows¹. From Figs. 3.12, 3.14 and 3.16, it can be seen that as α becomes smaller, the better the numerical values fit the Gaussian form. However, the fit starts resembling a parabolic shape as well.

From these figures, it can be seen that η_{tcc} decreases as β grows. This implies that the polymer is most confined in the case of two coaxial cones, and therefore ‘escapes’ further from the tips of the cones. An interesting feature we can note comparing between the figures, is that while the difference between the maximal and minimal η_{tcc} , i.e. $\eta_{tcc}^{max} - \eta_{tcc}^{min}$, monotonically decreases with α , the ratio $\frac{\eta_{tcc}^{max}}{\eta_{tcc}^{min}}$ remains of fixed value of $\simeq 1.83$ for all α . This implies that the affect of the tilting is more significant for large opening angles, as can be seen in Figs. 3.13, 3.15 and 3.17. These

α	a_0	a_1	a_2	χ_{red}^2
$\pi/5$	0.582 (0.548, 0.616)	0.48 (0.447, 0.512)	8.17 (6.63, 9.71)	0.87
$\pi/10$	0.286 (0.268, 0.304)	0.319 (0.303, 0.336)	2.72 (2.43, 3.02)	0.78
$\pi/20$	0.077 (0.035, 0.119)	0.344 (0.303, 0.385)	0.962 (0.798, 1.12)	0.51

Table 3.1: Fitting coefficients values for the fits in Figs. 3.12, 3.14 and 3.16, according to equation (3.27). The main number in each cell is the coefficient value, where the numbers in the parentheses show 95% confidence interval for the coefficient. The last column shows χ_{red}^2 parameter.

¹ χ_{red}^2 is calculated according to $\chi_{red}^2 = \frac{1}{\nu} \sum_i \left(\frac{f(x_i) - y(x_i)}{\sigma_i} \right)^2$, where $\nu = N - k - 1$ are the degrees of freedom, with N the number of points in the data and k the number of free parameters, x_i and y_i being the data points, $f(x_i)$ the value of the fit at point x_i and σ_i is the error in the data points.

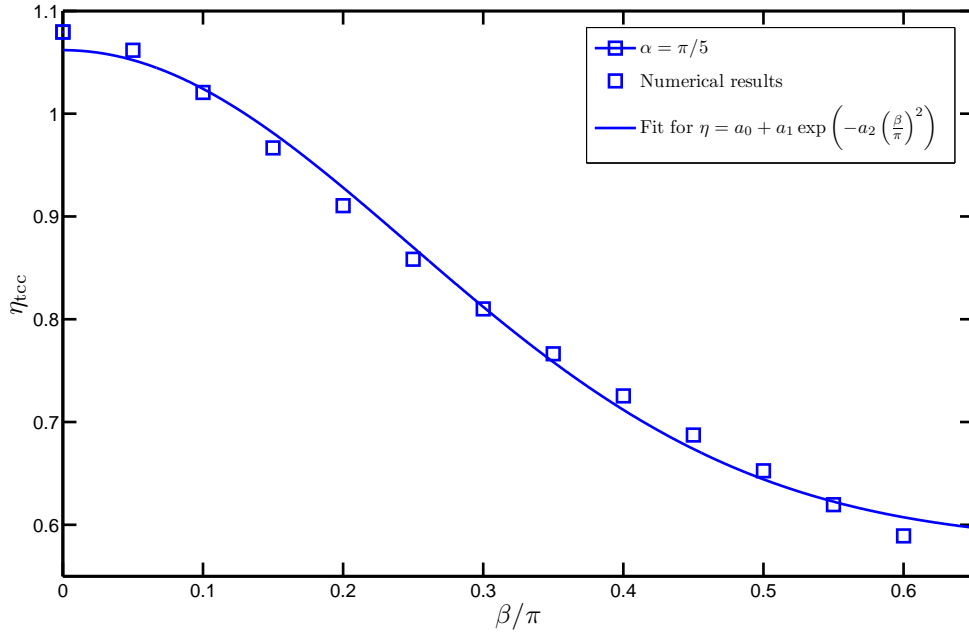


Figure 3.12: Plot of η_{tcc} (blue squares) as function of β for an ideal polymer between two cones with $\alpha = \pi/5$, as depicted in Fig. 3.9(b). Error bars are too small to be shown. Blue solid line shows rather poor Gaussian fit according to equation (3.27). Fit coefficient values are shown in Table 3.1.

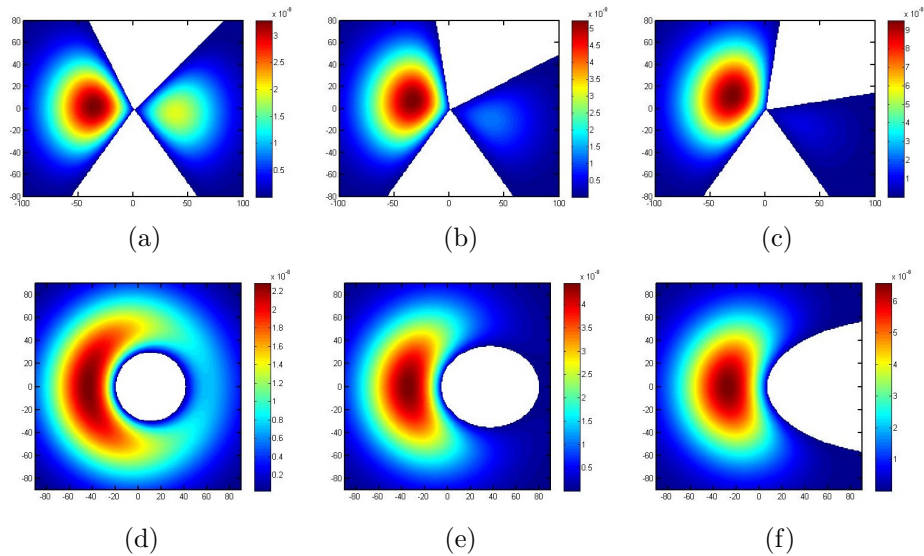


Figure 3.13: Vertical (top row) and horizontal (bottom row) cross sections of $P(\vec{R}, N)$ for an ideal polymer with $N = 4000$ between two cones with $\alpha = \pi/5$ (Fig. 3.9(b)). The top cone is tilted by angles $\beta = 0.05\pi$ (left column), $\beta = 0.15\pi$ (middle column) and $\beta = 0.25\pi$ (right column). (a)-(c) Show vertical cross sections of the $x - z$ plane, where (d)-(f) show horizontal cross sections of the $z = 40$ plane.

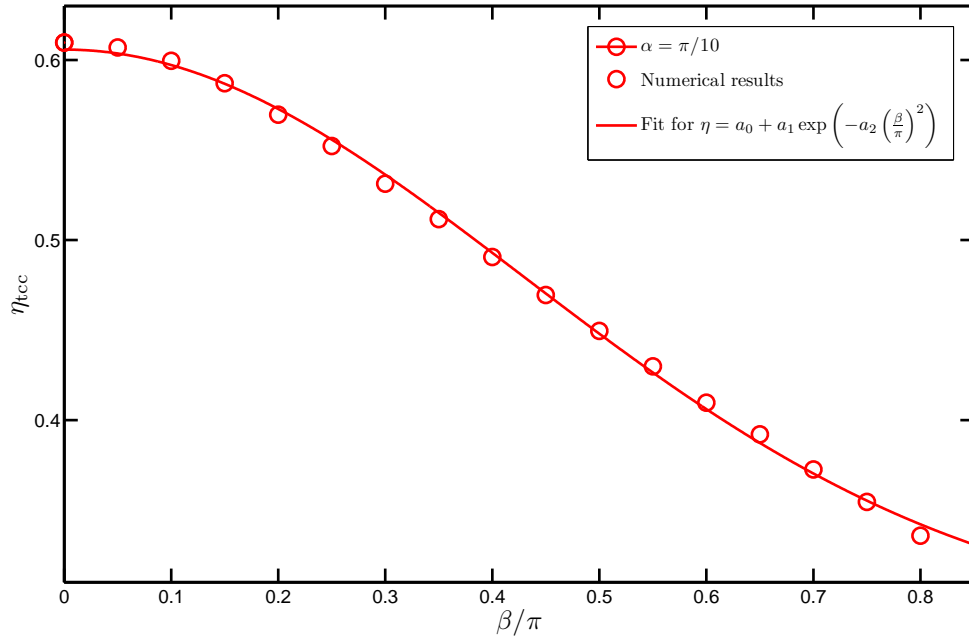


Figure 3.14: Plot of η_{tcc} (red circles) as function of β for an ideal polymer between two cones with $\alpha = \pi/10$, as depicted in Fig. 3.9(b). Error bars are too small to be shown. Red solid line shows Gaussian fit according to equation (3.27). Fit coefficient values are shown in Table 3.1.

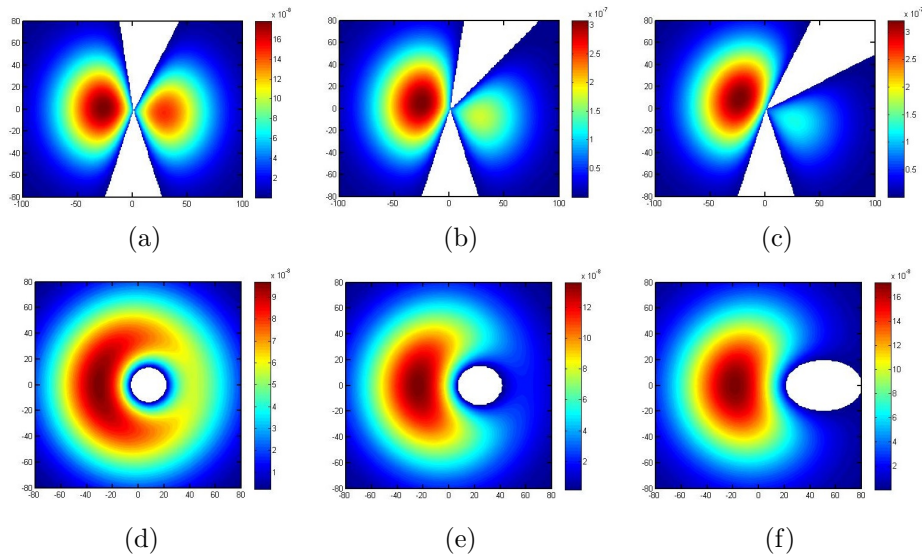


Figure 3.15: Vertical (top row) and horizontal (bottom row) cross sections of $P(\vec{R}, N)$ for an ideal polymer with $N = 4000$ between two cones with $\alpha = \pi/10$ (Fig. 3.9(b)). The top cone is tilted by angles $\beta = 0.05\pi$ (left column), $\beta = 0.15\pi$ (middle column) and $\beta = 0.25\pi$ (right column). (a)-(c) Show vertical cross sections of the $x - z$ plane, where (d)-(f) show horizontal cross sections of the $z = 40$ plane.

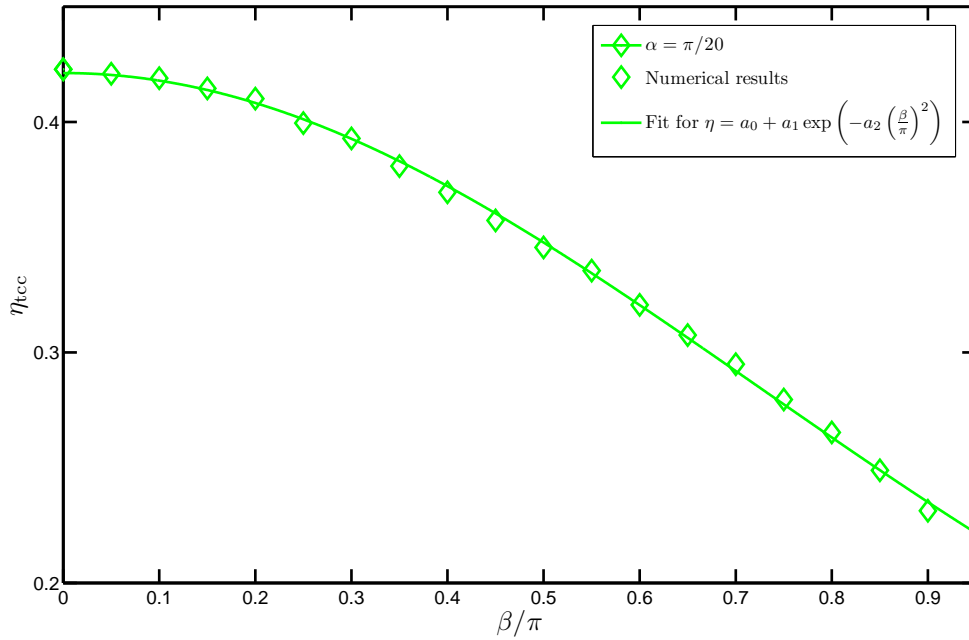


Figure 3.16: Plot of η_{tcc} (green diamonds) as function of β for an ideal polymer between two cones with $\alpha = \pi/20$, as depicted in Fig. 3.9(b). Error bars are too small to be shown. Green solid line shows good Gaussian fit according to equation (3.27), although it is quite similar to a parabolic shape. Fit coefficient values are shown in Table 3.1.

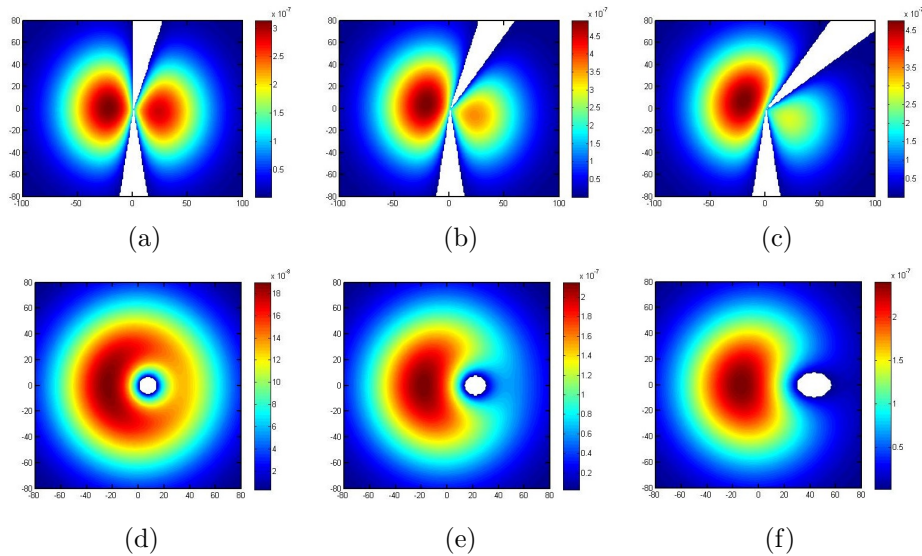


Figure 3.17: Vertical (top row) and horizontal (bottom row) cross sections of $P(\vec{R}, N)$ for an ideal polymer with $N = 4000$ between two cones with $\alpha = \pi/20$ (Fig. 3.9(b)). The top cone is tilted by angles $\beta = 0.05\pi$ (left column), $\beta = 0.15\pi$ (middle column) and $\beta = 0.25\pi$ (right column). (a)-(c) Show vertical cross sections of the $x - z$ plane, where (d)-(f) show horizontal cross sections of the $z = 40$ plane.

figures show horizontal and vertical cross sections of $P(\vec{R}, N)$ and we can see that the polymer ‘escapes’ to the ‘wider’ side of the cones. While for small α the difference between the probability density on both sides of the x -axis is not significant, as α and β grows, this phenomenon is much more noticeable. Therefore, the conformation of the polymer is more affected by the tilting of wide cones. Combined with what we see in the plots, we can conclude that the polymer is most confined when the cones are coaxial, and as one cone is tilted, the polymer ‘escapes’ to the wider side, where it is less confined, resulting in lower value of η_{tcc} .

3.4.3 Two Touching Cones

The last two-cones configuration we look at is a particular case of the above for $\beta = \pi - 2\alpha$, as depicted in Fig. 3.18(a). This setup is interesting, since we can compare it to the case of a single cone with opening angle 2α and to an elliptic cone defined by opening angles α and 2α . Since the horizontal cross section of the two touching cones resembles that of an elliptic cone (Fig. 3.18(b)), by investigating the differences between the conformations of a polymer in these configurations, we can better understand the influence of the probe shape on the conformations. We want to investigate whether the polymer ‘uses’ the free space between the cones (blue area in 3.18(b)), or perhaps the extra space the two circles capture (gray area in Fig. 3.18(b)) will have greater influence on the conformation. For the case of a single circular cone, we expect η to be larger, since the single cone captures much more space, as can be seen in Fig. 3.18(c). We expect the values of η in the two touching cones case to be similar to those of an elliptic cone. For small opening angles, we

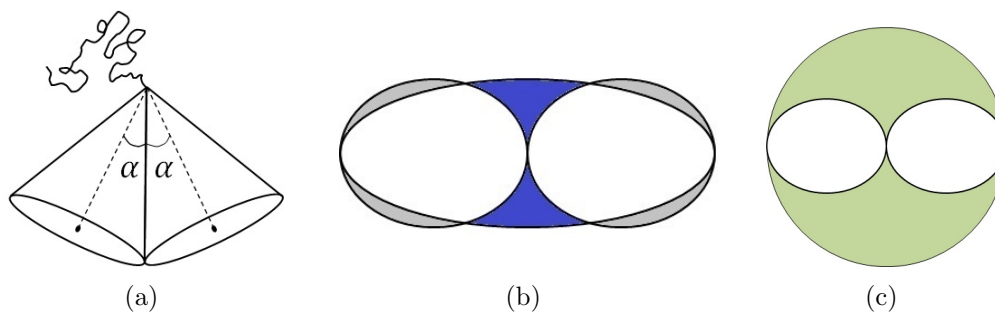


Figure 3.18: (a) Two touching circular cones with opening angles α . (b) Comparison between the cross sections of two touching circular cones and an elliptic cone with opening angles α and 2α . (c) Comparison between the cross sections of two touching circular cones and a single circular cone with opening angle 2α .

can assume all three configurations will show similar or even identical values of η .

Fig. 3.19 shows numerical values of η_{lcc} (“lcc” for lying-cone-cone), η_{ellip} (“ellip” for elliptic cone) and η_c as function of α . It can be seen that the single cone configuration differs from the two touching cones configuration, as values of η_c are larger than η_{lcc} even for small opening angles. This behavior was expected, since the single cone occupies much more space, causing the polymer to stretch further from the tip and leading to larger η_c . However, it can be seen that the elliptic cone configuration is more related to the two connected cones. For small angles, these two configurations are practically the same, as can be seen from the similarity between η_{lcc} and η_{ellip} . However, the difference between η_{lcc} and η_{ellip} increases with α , where $\eta_{\text{lcc}} \geq \eta_{\text{ellip}}$ for all α . This implies that the two touching cones ‘repel’ the polymer further away from the tip. This feature is somewhat surprising.

To understand better the geometries, we can look at the volume V and lateral surface area S of the two configurations:

$$V_{\text{lcc}} = \frac{2\pi}{3}H^3 \tan \alpha \quad S_{\text{lcc}} = 2\pi H^2 \frac{\tan \alpha}{\cos \alpha}, \quad (3.28)$$

$$V_{\text{ellip}} = \frac{\pi}{3}H^3 \tan 2\alpha \tan \alpha \quad S_{\text{ellip}} = 2H^2 \frac{\tan 2\alpha}{\cos \alpha} E \left(\cos \alpha \sqrt{1 + \frac{\tan^2 \alpha}{\tan^2 2\alpha}} \right), \quad (3.29)$$

where H is the height of the cone ($H \gg \sqrt{\langle R^2 \rangle}$) and $E(x)$ is the complete elliptic integral of the second kind [26]. Since for our configuration $\alpha < \pi/4$, from the above relations it follows that:

$$\begin{aligned} V_{\text{ellip}} &> V_{\text{lcc}} && \text{for } \alpha < \frac{\pi}{4}, \\ S_{\text{ellip}} &< S_{\text{lcc}} && \text{for } \alpha \lesssim 0.15\pi, \\ S_{\text{ellip}} &> S_{\text{lcc}} && \text{for } \alpha \gtrsim 0.15\pi. \end{aligned} \quad (3.30)$$

From the relations in (3.30), it can be seen that for $\alpha > 0.15\pi$, both the volume and lateral surface area of the elliptic cone are larger than the two touching cones. However, Fig. 3.19 shows that $\eta_{\text{lcc}} > \eta_{\text{ellip}}$ for all α . This implies that neither measure is directly affecting the conformation of the polymer.

By looking at the cross sections of $P(\vec{R}, N)$ for these configurations (Figs. 3.20, 3.21 and 3.22), we can see that the probability densities are identical for the two touching cones and the elliptic cone for $\alpha = 0.01\pi$ and look very similar in the case of $\alpha = 0.1\pi$. However, there is some difference between the two configurations

for $\alpha = 0.2\pi$. We can also note that the values of the probability for elliptic cone are larger than those in parallel areas for the two cones, for all α . This implies that the two cones ‘absorbs’ more optional conformations, resulting in larger end-to-end distance. For large opening angles, e.g. $\alpha = 0.2\pi$, $P(\vec{R}, N)$ seems to be more ‘smeared’ in the elliptic cone case (Figs. 3.22(g)-(i)) than in the two cones case, where the polymer’s end seems to be more localized (Figs. 3.22(a)-(c)). Vertical cross sections of $P(\vec{R}, N)$ away from the cones axis show similar behavior (Figs. 3.22(e)-(f) and Figs. 3.22(k)-(l)).

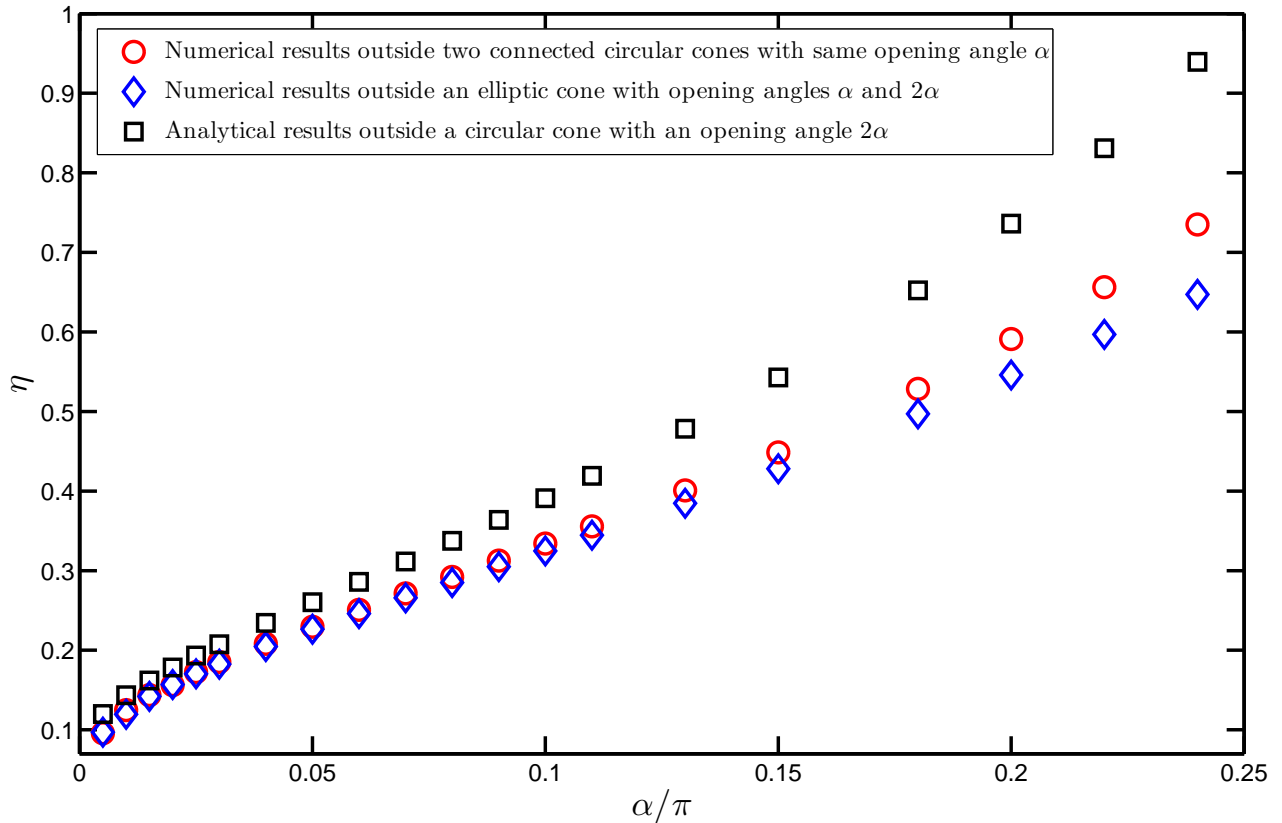


Figure 3.19: Numerical values of η_{cc} (red circles), η_{ellip} (blue diamonds) and analytical values of η_{c} (black squares) as function of α . The opening angle of the two touching cones is α , the elliptic cone is defined by opening angles α and 2α and the single circular cone has opening angle 2α (see Fig. 3.18).

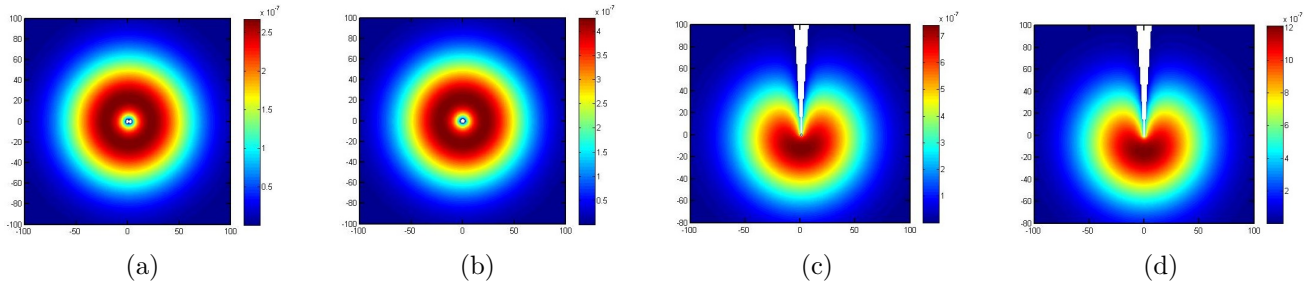


Figure 3.20: Cross sections of $P(\vec{R}, N)$ for an ideal polymer attached to the tip of two connected circular cones ((a) and (c)) and elliptic cone ((b) and (d)), for $\alpha = 0.01\pi$ and $N = 4000$. α is defined as the opening angle of the two circular cones, where the elliptic cone opening angles are α and 2α . Horizontal cross sections (left images) show the $z = 40$ plane. Vertical cross sections (right images) show the $x - z$ plane. It can be seen that the probability density looks identical in both cases and very similar to that of a circular cone.

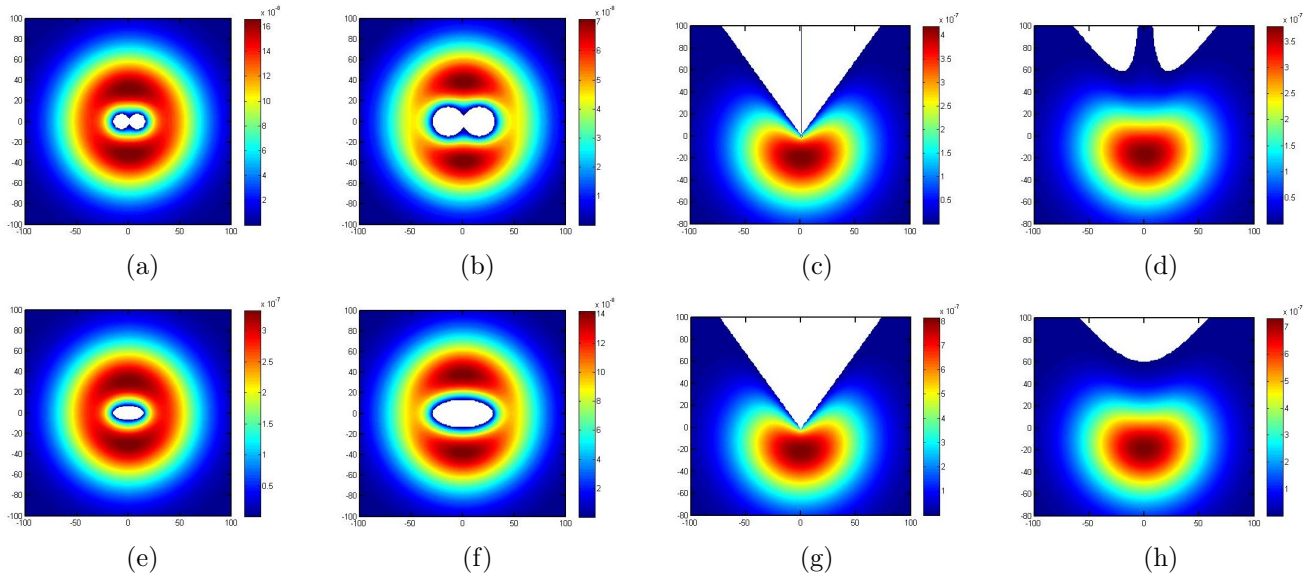


Figure 3.21: Cross sections of $P(\vec{R}, N)$ for an ideal polymer attached to the tip of two connected circular cones (top row) and elliptic cone (bottom row), for $\alpha = 0.1\pi$ and $N = 4000$. α is as defined in Fig. 3.20. Horizontal cross sections (left images) show the $z = 20$ plane ((a) and (e)) and $z = 40$ plane ((b) and (f)). Vertical cross sections (right images) show the $x - z$ plane ((c) and (g)) and $y = 20$ plane ((d) and (h)). While the probability densities in the two cases are similar, some differences can be noted, especially in the horizontal cross sections where the density around the two cones is more centered than that around the elliptic cone.

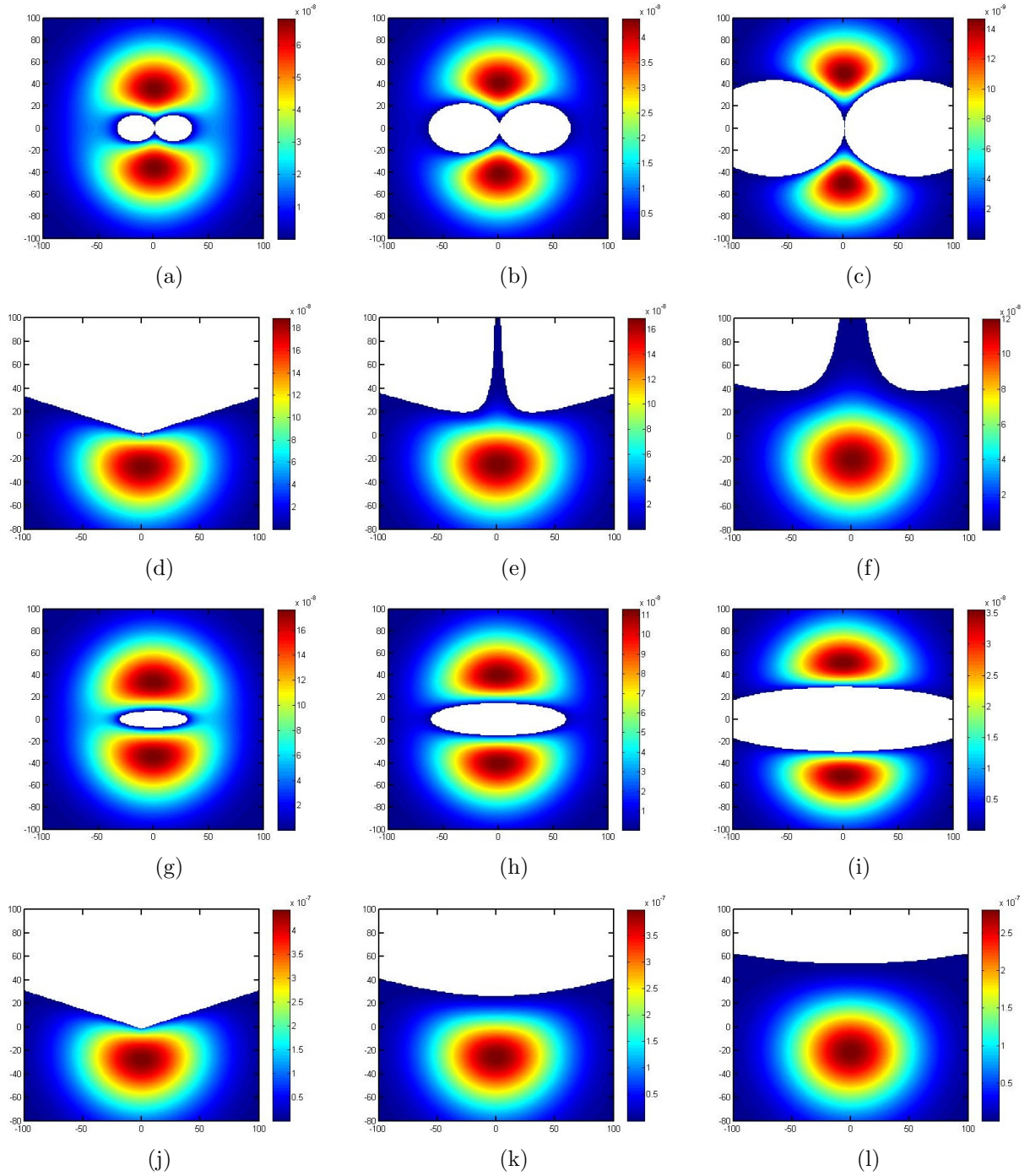


Figure 3.22: Cross sections of $P(\vec{R}, N)$ for an ideal polymer attached to the tip of two connected circular cones (two top rows) and elliptic cone (two bottom rows), for $\alpha = 0.2\pi$ and $N = 4000$. α is as defined in Fig. 3.20. Horizontal cross sections show the $z = 10$ plane ((a) and (g)), $z = 20$ plane ((b) and (h)) and $z = 40$ plane ((c) and (i)). Vertical cross sections show the $x - z$ plane ((d) and (j)), $y = 20$ plane ((e) and (k)) and $y = 40$ plane ((f) and (l)). The difference between the probability densities in the two configurations is obvious both in the vertical and horizontal cross sections, where it is best noticeable far from the cones' tips (right column).

Chapter 4

Cone-Plane Configurations

In this chapter, we investigate an ideal polymer attached to the tip of a circular cone in the vicinity of an impenetrable plane in three dimensions. We use the method described in Section 3.1 to derive numerical values of η . We start with an ideal polymer attached to the tip of a circular cone perpendicular to the plane, a case we can solve analytically [21]. We then tilt the cone and find the values of η numerically.

4.1 Ideal Polymer Between an Upright Cone and a Plane

We start by looking at an ideal polymer attached to the tip of a circular cone perpendicular to an impenetrable plane, as depicted in Fig. 4.1. In order to derive η_{cp} (“cp” for cone-plane) as a function of the opening angle of the cone α , we follow the same path as in the two cones configuration, described in equations (3.19) - (3.21), and find the angular function $g(\theta)$ in $P(\vec{R}, N)$. For this case, we need to solve equation (3.20):

$$(1 - \mu^2) \frac{d^2 g}{d\mu^2} - 2\mu \frac{dg}{d\mu} + \eta(\eta + 1)g = 0,$$

under the boundary conditions $g(\alpha) = g(\pi/2) = 0$. The condition $g(\pi/2) = 0$ corresponds to $\mu = 0$ and yields the ratio [21]:

$$\frac{a_2}{a_1} = -\frac{P_\eta(0)}{Q_\eta(0)} = \frac{2}{\pi \tan(\pi\eta/2)}, \quad (4.1)$$

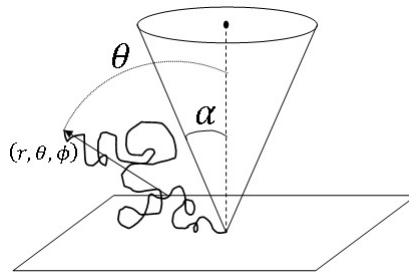


Figure 4.1: An ideal polymer attached to the tip of a circular cone with opening angle α , near an impenetrable plane.

where P_μ and Q_μ are the regular Legendre functions. Therefore, we can set the angular function to be:

$$g(\theta) = \pi \sin\left(\frac{\pi\eta}{2}\right) P_\eta(\cos\theta) + 2 \cos\left(\frac{\pi\eta}{2}\right) Q_\eta(\cos\theta). \quad (4.2)$$

As seen in the previous chapter, the exponent η_{cp} is the smallest η satisfying the condition $g(\alpha) = 0$. The values of η_{cp} as a function of α can be extracted numerically and are plotted in Fig. 4.2.

Since the initial position of the diffuser cannot be on either the tip of the cone or the plane, the distance between the cone and the plane is set to be $2a$, and the initial point is at distance a from each of the objects. Fig. 4.2 shows comparison between numerical and analytical values of η_{cp} as function of α , where excellent correspondence can be seen. However, magnification reveals small discrepancy of $\sim 0.5\%$. This discrepancy is due to the discretization of the lattice and will serve us for the evaluation of errors in the next section. Fig. 4.3 displays vertical cross section of $P(\vec{R}, N)$. It shows the azimuthal symmetry which allowed us to disregard the dependence of $P(\vec{R}, N)$ in ϕ .

4.2 Ideal Polymer Between a Tilted Cone and a Plane

4.2.1 Tilted Cone near a Plane

We look at the same setup as in the previous Section, only now we tilt the cone by angle β with respect to the z -axis (Fig. 4.4(a)). Since the azimuthal symmetry is lost, we cannot find $P(\vec{R}, N)$ analytically. Therefore, we find numerically η_{tcp} (“tcp” for tilted-cone-plane) as function of β for $\alpha = \pi/5$, $\alpha = \pi/10$ and $\alpha = \pi/20$.

Figs. 4.5 and 4.6 show vertical and horizontal cross sections of $P(\vec{R}, N)$, respectively, for $\alpha = \pi/5$ and $\alpha = \pi/10$ and three different β s. By looking at these figures, it can be noticed that even for a slight tilt of the cone, the polymer ‘escapes’ to the wider side, where it has more room to propagate. For larger tilting angles, the polymer is much less likely to be found in the narrower side. As α grows, this effect is even more prominent, due to the fact that according to our notation, the same tilting angle allows less space for the polymer to propagate in the narrower side of the cone.

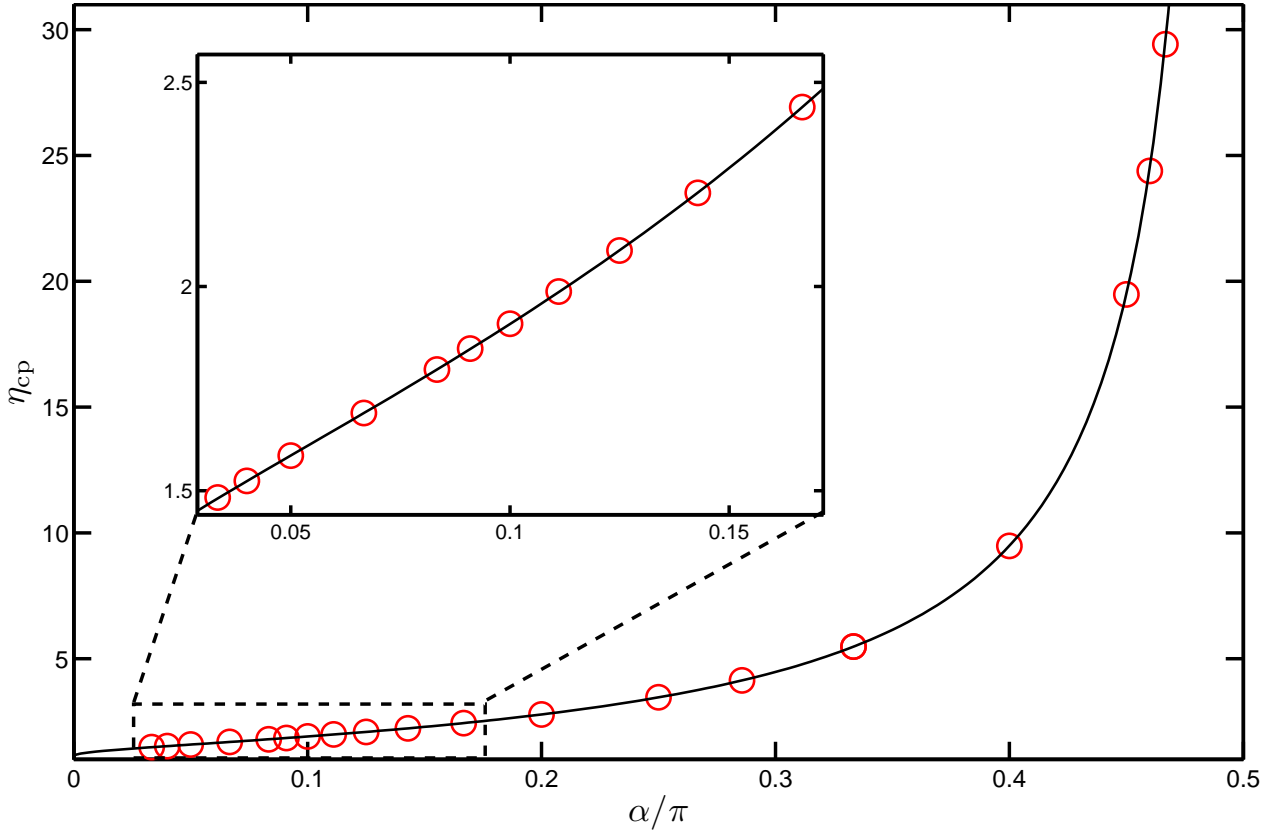


Figure 4.2: Plot of η_{cp} as function of α . Red circles show numerical values of η_{cp} , while the black solid line shows analytical values acquired from finding the lowest root of the angular function in (4.2). Excellent correspondence between numerical and analytical values of η_{cp} can be seen. For $\alpha = \pi/2$ we get divergence of η_{cp} , as expected in this case. Error bars are too small to be shown.

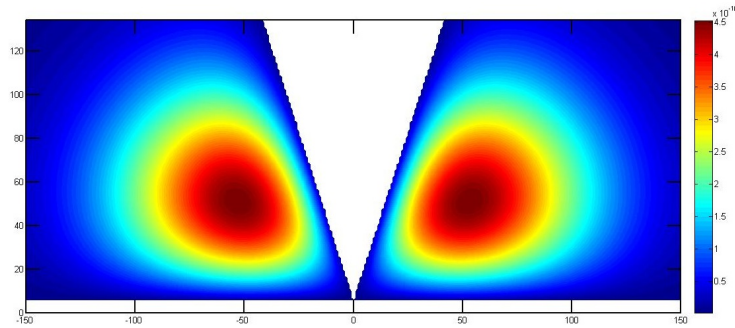


Figure 4.3: Vertical cross section of $P(\vec{R}, N)$ for an ideal polymer attached to the tip of a circular cone touching a plane (Fig. 4.1). The cross section is on the $x - z$ plane, for $N = 8000$ and $\alpha = \pi/10$.

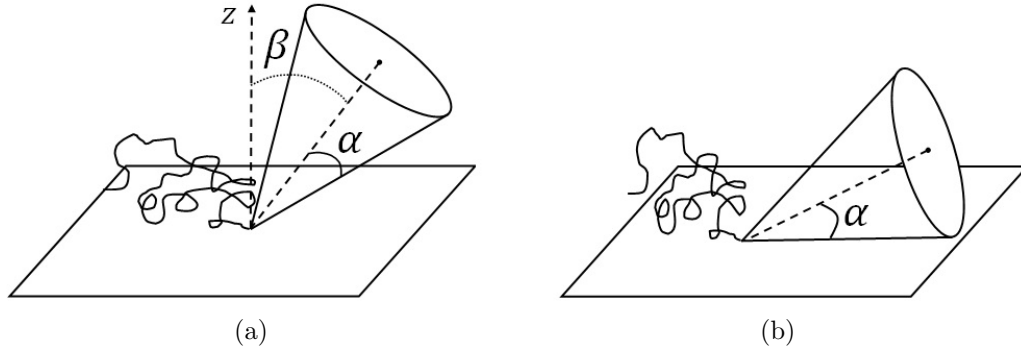


Figure 4.4: An ideal polymer attached to the tip of a circular cone with opening angle α , (a) tilted by angle β near an impenetrable infinite plane (denoted by “tcp”), and (b) lying on the plane, meaning $\beta = \pi/2 - \alpha$ (denoted by “lcp”).

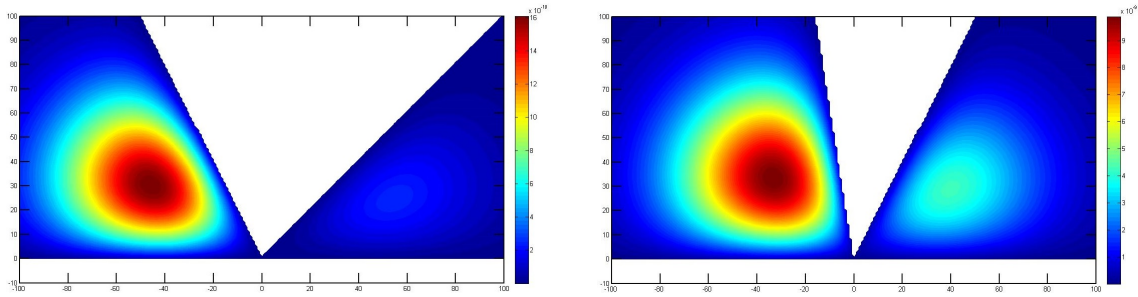
Numerical values of η_{tcp} as function of β for $\alpha = \pi/5$, $\alpha = \pi/10$ and $\alpha = \pi/20$, are shown in Figs. 4.7, 4.8 and 4.9, respectively. From the maximal discrepancy seen in the previous Section, we approximate the error to be 1% of the value, meaning $\Delta\eta_{\text{tcp}} = 0.01\eta_{\text{tcp}}$ (see Appendix A). Since the cone-plane configuration is in fact a particular case of the two cones, with one of the cones open with $\alpha_2 = \pi/2$ (Fig. 3.9(a)), we can follow the same path as done earlier and approximate the numerical values by a Gaussian fit (Eq. (3.27)):

$$\eta_{\text{tcp}}(\beta) = a_0 + a_1 \exp \left\{ -a_2 \left(\frac{\beta}{\pi} \right)^2 \right\}.$$

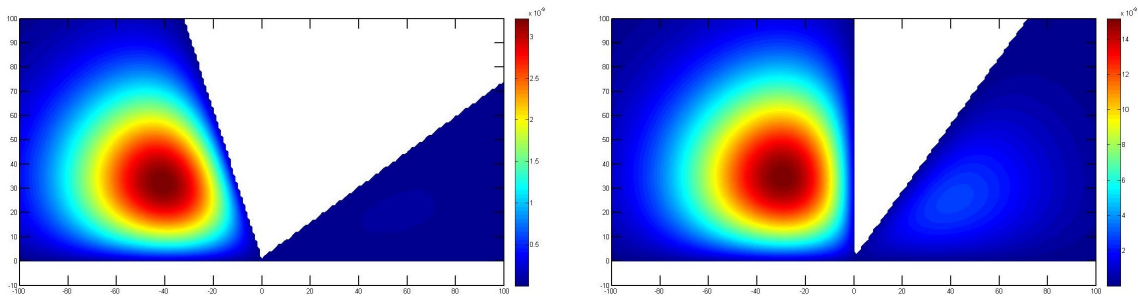
The fitting curves are shown by solid lines in Figs. 4.7, 4.8 and 4.9. Fit coefficients a_i are shown in Table 4.1.

Cone opening angle	a_0	a_1	a_2	χ_{red}^2
$\pi/5$	1.57 (1.44, 1.71)	1.16 (1.01, 1.31)	48.1 (30.4, 65.9)	2.96
$\pi/10$	1.16 (1.1, 1.21)	0.73 (0.67, 0.78)	23.9 (18.6, 29.1)	4.11
$\pi/20$	1.04 (1, 1.07)	0.53 (0.5, 0.57)	16.7 (13.5, 19.9)	1.56

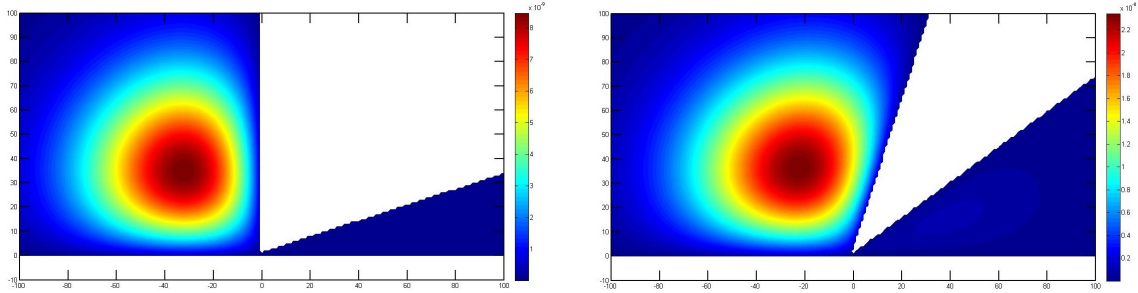
Table 4.1: Fitting coefficients values for the fits in Figs. 4.7, 4.8 and 4.9, according to equation (3.27). The main number in each cell is the coefficient value, where the numbers in the parentheses show 95% confidence interval for the coefficient. The last column shows the χ_{red}^2 parameter, as defined in previous Chapter.



(a) Vertical cross section of $P(\vec{R}, N)$ for $\beta = 0.05\pi$.

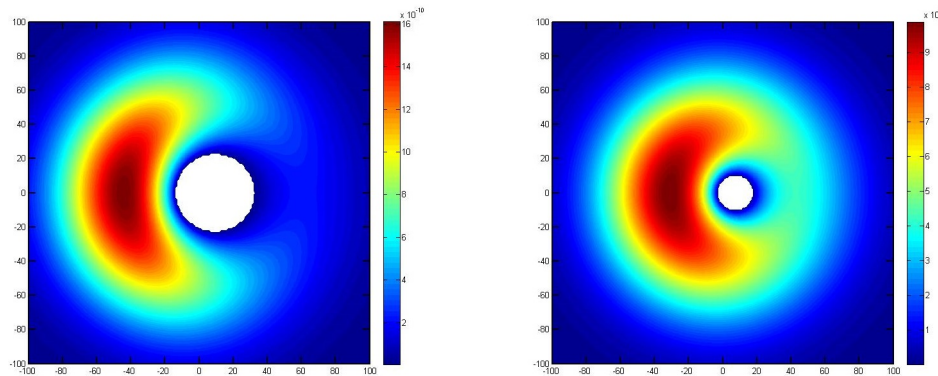


(b) Vertical cross section of $P(\vec{R}, N)$ for $\beta = 0.1\pi$.

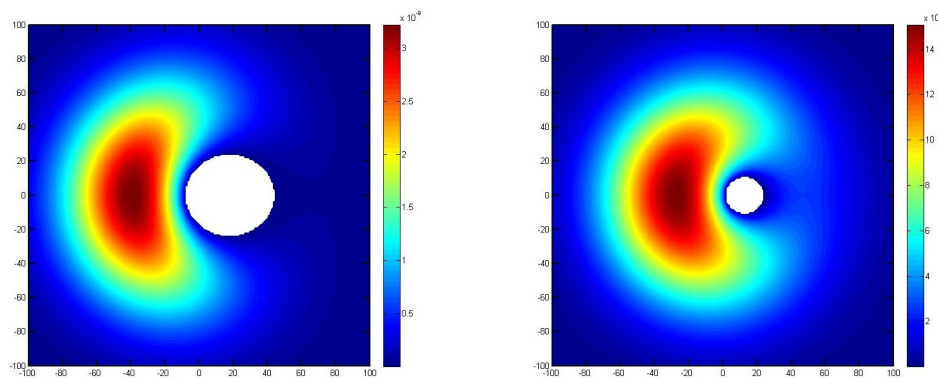


(c) Vertical cross section of $P(\vec{R}, N)$ for $\beta = 0.2\pi$.

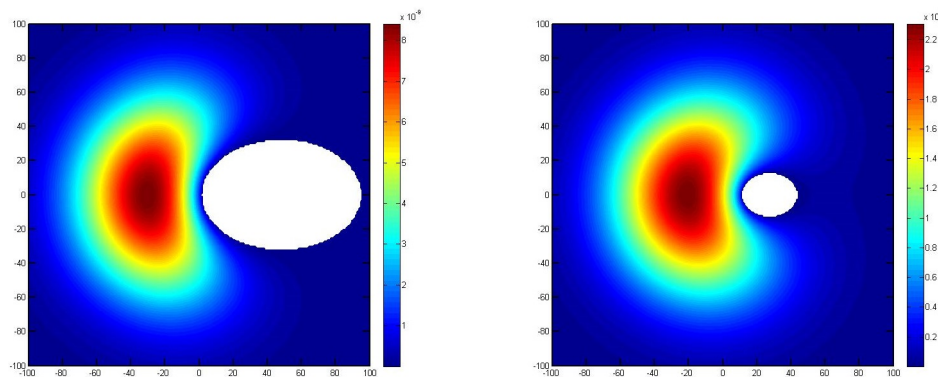
Figure 4.5: Vertical cross sections of $P(\vec{R}, N)$ for a polymer attached to the tip of a tilted cone touching a plane (Fig. 4.4(a)). The vertical cross sections are on the $x - z$ plane for $N = 4000$. The tilting angles are (a) $\beta = 0.05\pi$, (b) $\beta = 0.1\pi$ and (c) $\beta = 0.2\pi$. The left column shows the density for $\alpha = \pi/5$ and the right column shows it for $\alpha = \pi/10$. It can be seen that for $\alpha = \pi/10$ there is significant probability for the polymer's end to be located on the narrower side of the cone for small β . However, when α is larger, the probability of the polymer ending on the narrow side becomes negligible even for small tilting angles, as can be seen in (a) and (b). For larger β , as can be seen in (c), the polymer 'escapes' to the wider side of the cone, regardless of its opening angle.



(a) Horizontal cross section of $P(\vec{R}, N)$ for $\beta = 0.05\pi$.



(b) Horizontal cross section of $P(\vec{R}, N)$ for $\beta = 0.1\pi$.



(c) Horizontal cross section of $P(\vec{R}, N)$ for $\beta = 0.2\pi$.

Figure 4.6: Horizontal cross sections of $P(\vec{R}, N)$ for a polymer attached to the tip of a tilted cone touching a plane (Fig. 4.4(a)). The horizontal cross sections are on the $z = 30$ plane for $N = 4000$. The tilting angles are (a) $\beta = 0.05\pi$, (b) $\beta = 0.1\pi$ and (c) $\beta = 0.2\pi$. The left column shows the density for $\alpha = \pi/5$ and the right column shows it for $\alpha = \pi/10$. These figures complete the picture described in Fig. 4.5. It can be seen that the larger β is, the more the polymer ‘escapes’ to the wider side of the cone.

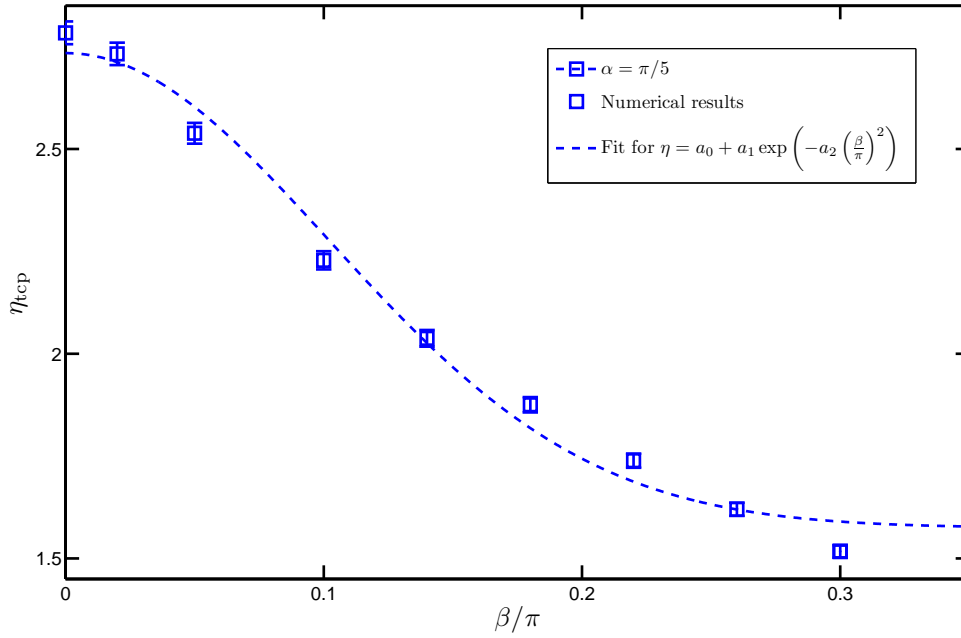


Figure 4.7: Plot of η_{tcp} as function of β for $\alpha = \pi/5$. The blue squares show numerical values of η_{tcp} , where the blue dashed line shows fit to equation (3.27). Fit coefficients values can be found in table 4.1. It can be seen that the fit does not match the numerical points as well as we saw in the two cones case.

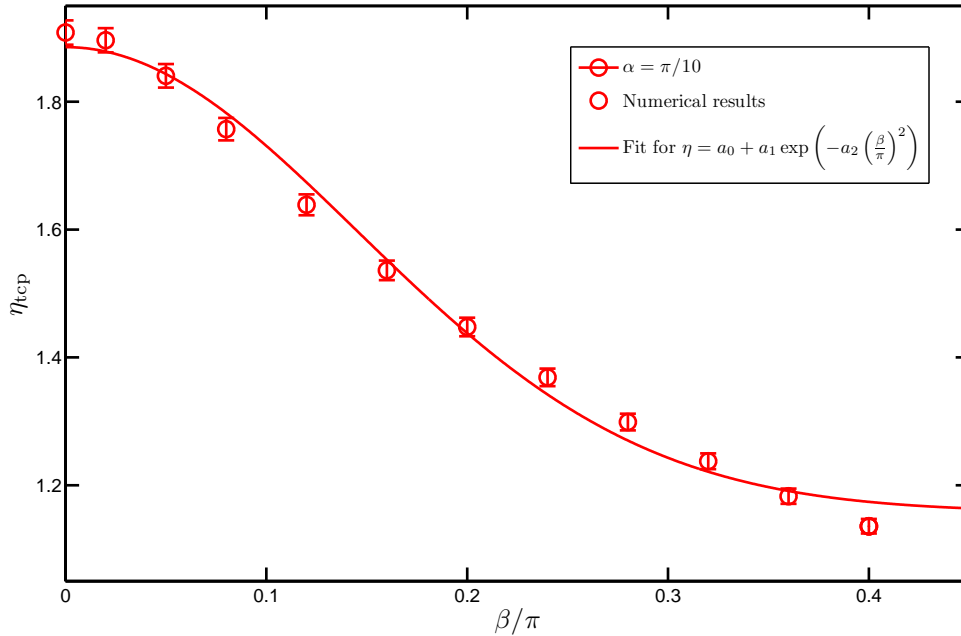


Figure 4.8: Plot of η_{tcp} as function of β for $\alpha = \pi/10$. The red circles show numerical values of η_{tcp} , where the red solid line shows fit to equation (3.27). Fit coefficients values can be found in table 4.1. It can be seen that the fit does not match the numerical points very well, although it is better than for $\alpha = \pi/5$ (Fig. 4.7).

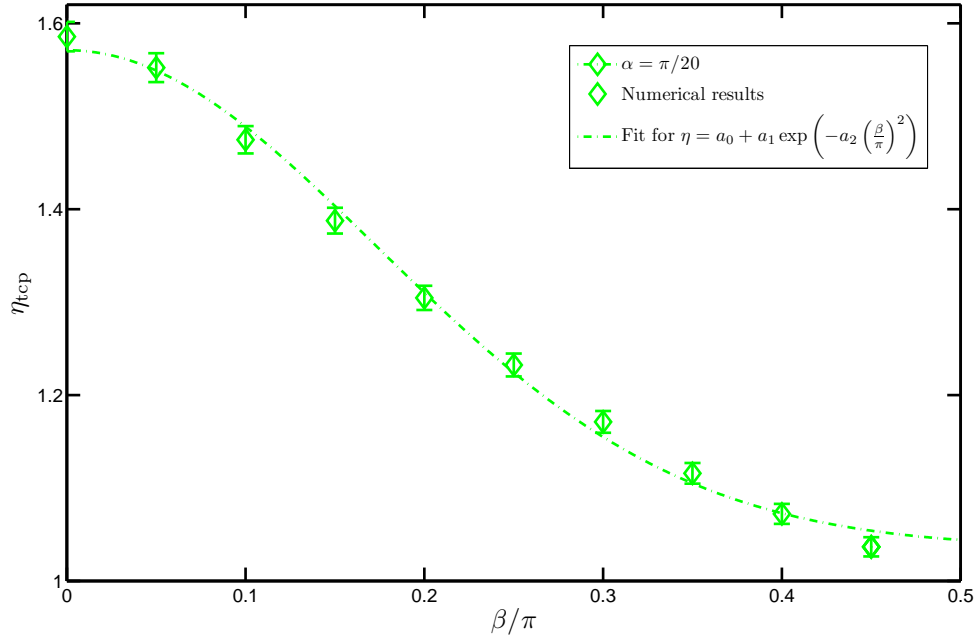


Figure 4.9: Plot of η_{tcp} as function of β for $\alpha = \pi/20$. The green diamonds show numerical values of η_{tcp} , where the green dashed-dotted line shows fit to equation (3.27). Fit coefficients values can be found in table 4.1. The fit gives better description of the numerical results than in the previous cases.

All figures show same behavior as seen in the tilted cone - upright cone case. As expected, η_{tcp} is maximal for $\beta = 0$, where the cone is perpendicular to the plane, and is minimal for $\beta = \pi - \alpha$. This property is related to the fact that when the cone is tilted, the polymer ‘escapes’ to the wider side, where it has more room to propagate, leading to smaller $\langle R^2 \rangle$ and smaller value of η . The Gaussian fit does not give good description for the results for large α , as seen in Fig. 4.7. The fit becomes better as α becomes smaller. This implies that the chosen function may not be suitable for large opening angles, though the general behavior resembles that of a Gaussian. The change in η_{tcp} is more moderate when α becomes smaller, meaning the tilting of the cone has less effect on the conformation of the polymer. On the other hand, for large opening angles, even a slight tilt of the cone determines the side the polymer ‘chooses’ with great confidence, resulting in a more rapid change of η_{tcp} . This is interesting since unlike the case of two cones, the ratio $\frac{\eta_{\text{tcp}}^{\text{max}}(\alpha)}{\eta_{\text{tcp}}^{\text{min}}(\alpha)}$ depends on α and is $\simeq 1.83$ for $\alpha = \pi/5$, $\simeq 1.68$ for $\alpha = \pi/10$, and $\simeq 1.53$ for $\alpha = \pi/20$.

4.2.2 Cone Lying on a Plane

We now consider the case of $\beta = \pi - \alpha$, describing a polymer attached to the tip of a cone lying on the plane, as depicted in Fig. 4.4(b). Numerical values of η_{lcp} (“lcp” for lying-cone-plane) as function of α are shown in Fig. 4.10. The figure also shows analytical plot of η_{cp} (black line), taken from Fig. 4.2. It can be seen that our numerical results for the cone lying on a plane has the same shape as that of the cone-plane configuration. However, η_{lcp} is smaller than η_{cp} for every α . This means that the cone is less interrupting when it is lying on the plane and the polymer is less confined.

An interesting phenomenon can be noticed for small values of α . For the case of a lying cone on a plane, we can see almost no difference between a cone with small opening angle and a half-space configuration, where $\eta_{\text{hs}} = 1$. This implies that the polymer is ‘unaware’ of the small cone lying on the plane, and the geometry is practically half-space. However, when the cone is perpendicular to the plane, even for small α , the values of η_{cp} are significantly larger than 1. This means that even a small cone is affecting the conformation of the polymer when it is situated in the middle of the polymer’s propagation zone.

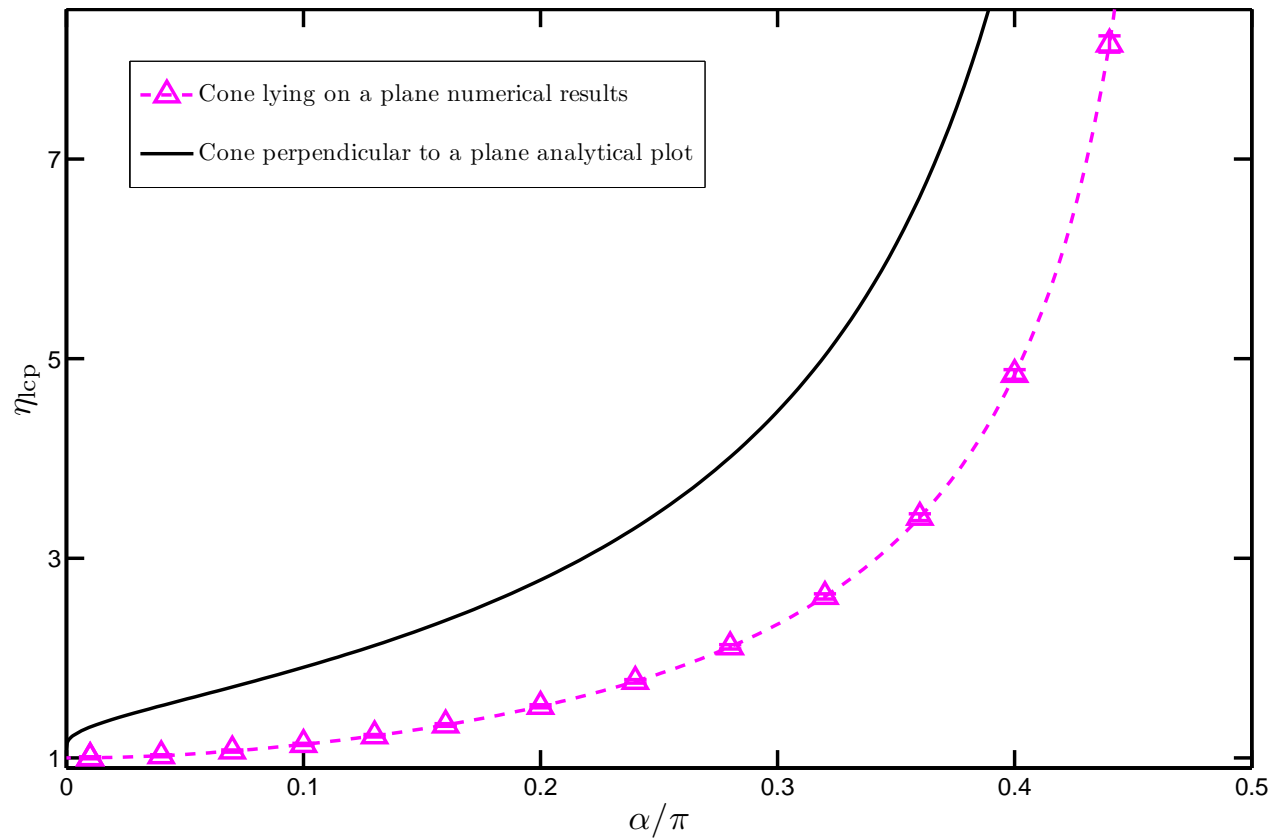


Figure 4.10: Numerical values of η_{cp} (purple triangles) as function of α for an ideal polymer attached to the tip of a cone lying on a plane (Fig. 4.4(b)). Dashed purple line is an interpolation for the numerical values and is shown only for convenience. The black solid line indicates analytical values of η_{cp} for the cone-plane configuration, taken from Section 4.1.

Chapter 5

Winding Angle Distributions

In this chapter we study the winding angle distribution of an ideal polymer attached to the tip of a cone in the vicinity of an impenetrable plane (Fig. 4.1), as described in Section 2.4. The numerical simulation method used in the previous chapters only gives information on the probability density of the end point of the polymer, and lacks information on each monomer location. Therefore, we start by introducing a different numerical simulation method that will be used in this chapter. We present numerical results for the dependence of the root-mean-square of the winding angle $\sqrt{\langle\Theta^2\rangle}$ on the number of monomers N , for a polymer connected to a circular rod and connected to a cone touching a plane. We investigate the winding angles of the last monomer, as well as several other monomers within the chain.

5.1 Monte Carlo Simulation

The main drawback of the discrete diffusion simulation method, described in Section 3.1, is that it gives only statistical information on the end point of the polymer, where all the information on the conformation is lost. Therefore, in order to find the winding angle of an intermediate monomer, a different numerical method is necessary. We use Metropolis importance sampling Monte Carlo simulation method [27, 28] to create conformation of ideal polymer and derive the winding angle distributions with respect to the polymer's length N in different geometries. Unlike the discrete diffusion simulation, this simulation method is done off-lattice and in continuum. This method is described in greater detail in Appendix B.

We consider the Gaussian chain model defined in Section 1.3.2, where the energy E_n is defined according to equation (1.12):

$$E_n = \frac{1}{2}k \sum_{n=1}^N \left(\vec{R}_n - \vec{R}_{n-1} \right)^2.$$

For numerical simplicity, we set the spring constant to $k = \frac{2k_B T}{a^2}$. We start with a possible conformation of an ideal polymer in some geometry and reach equilibrium state using the algorithm described in Appendix B. Once an equilibrium state is

achieved, we gather information on the winding angle of each atom. Repeating this scheme many times, allows us to generate statistics for the problem. Additional clarification regarding this method and its errors can be found in Appendix B.

5.2 Winding Angle Distributions of an Ideal Polymer Near a Circular Rod

We start by looking at an ideal polymer attached to an impenetrable infinite circular rod of radius l in three dimensions, as depicted in Fig. 5.1(a). As mentioned in Section 2.4, this problem has been previously solved by Rudnick and Hu [22], who found the linear relation:

$$\sqrt{\langle \Theta^2 \rangle} = a_0 \ln N + b_0, \quad (5.1)$$

with $a_0 = \frac{1}{\sqrt{12}} \simeq 0.289$.

By using the Monte-Carlo (MC) simulation method as described above, we extract the winding angle Θ for several polymer lengths N . Since the initial point cannot be located on the rod, we start with distance $r' = a$ away from the rod. Fig. 5.1(b) shows an overhead view of an ideal polymer with $N = 100$ near the rod. This figure shows a single conformation of the polymer after $t = 2N^2$ MC time units. Note that a MC time unit corresponds to N attempts of atom moves. For statistical analysis, we used 5000 conformations for each polymer length N .

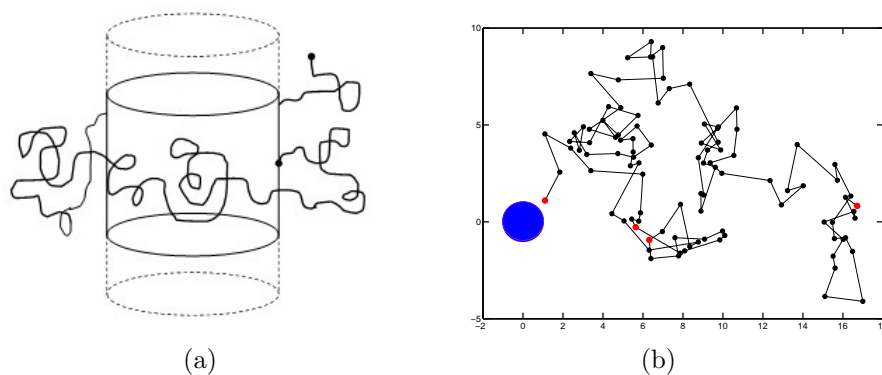


Figure 5.1: (a) An ideal polymer attached to an impenetrable infinite circular rod. The small dots mark the polymer ends. (b) Overhead look of an ideal polymer conformation in three dimensions in the vicinity of an impenetrable rod. The polymer conformation was created using the method described in Section 5.1 for $N = 100$. Red dots mark the first, 10th, 20th and last atoms in the chain.

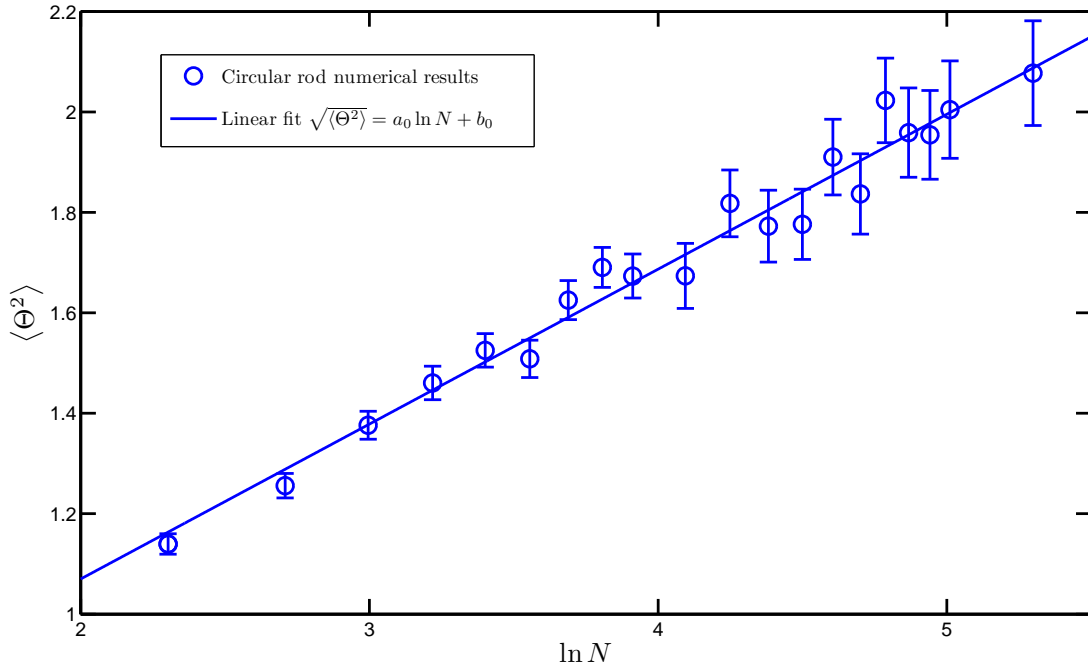


Figure 5.2: Plot of $\sqrt{\langle \Theta^2 \rangle}$ as function of $\ln N$ for an ideal polymer attached to a circular rod (Fig. 5.1(a)). Blue circles show numerical values, blue solid line shows linear fit according to (5.1). Equation (5.2) shows fit coefficients values.

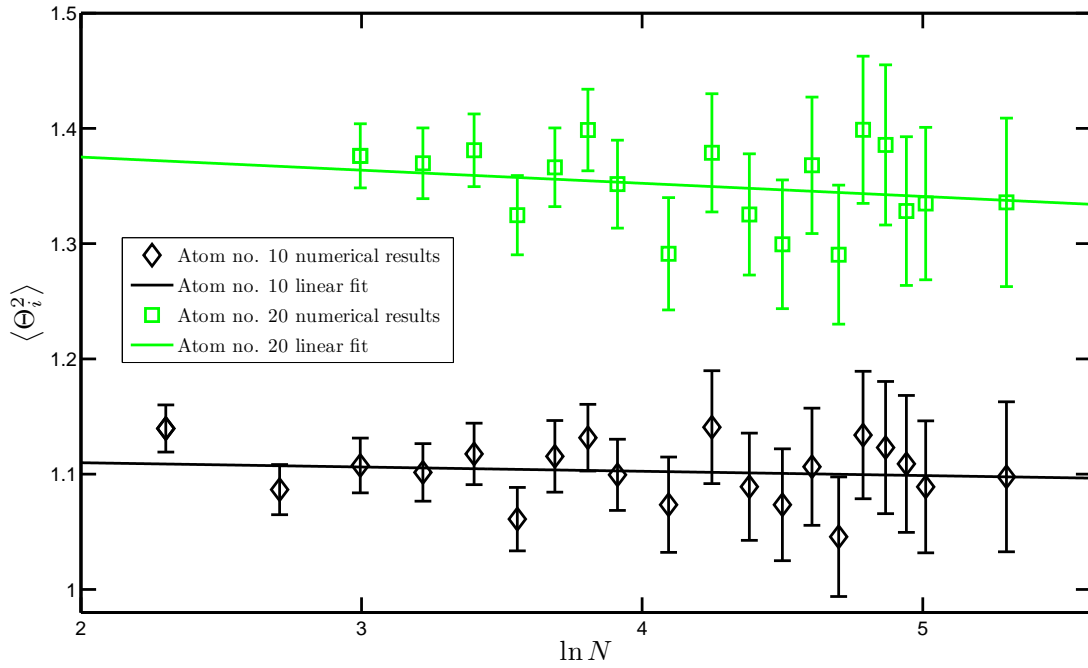


Figure 5.3: Plot of $\sqrt{\langle \Theta_{10}^2 \rangle}$ (black diamonds) and $\sqrt{\langle \Theta_{20}^2 \rangle}$ (green squares) as function of $\ln N$ for an ideal polymer attached to a circular rod. Solid lines show linear fits according to (5.3). Equation (5.4) shows fit coefficients values.

Fig. 5.2 shows numerical values of $\sqrt{\langle\Theta^2\rangle}$ as function of $\ln N$. Linear fit according to equation (5.1) yields:

$$a_0 = 0.308 \pm 0.031 \quad , \quad b_0 = 0.45 \pm 0.14. \quad (5.2)$$

It can be seen that the numerical value of a_0 is within error range of the analytical value, with relative error of 10%. By using the values of a_0 and b_0 found, we can find that the polymer will complete a single revolution around the rod, i.e. $\sqrt{\langle\Theta^2\rangle} = 2\pi$, only for $N \simeq 1.7 \cdot 10^8$. This means that the polymer does not surround the rod for our range of N s. This feature is uncertain, since our simulations are done only up to $N = 200$, and the linear relation may change for larger N .

We also study the dependence of $\sqrt{\langle\Theta_i^2\rangle}$ on the total number of monomers N , for intermediate atoms $i = 10$ and $i = 20$. The dependence of $\sqrt{\langle\Theta_{10}^2\rangle}$ and $\sqrt{\langle\Theta_{20}^2\rangle}$ on $\ln N$ is shown in Fig. 5.3. We fit the results according to equation (5.1), using different notations:

$$\begin{aligned} \sqrt{\langle\Theta_{10}^2\rangle} &= c_0 \ln N + d_0, \\ \sqrt{\langle\Theta_{20}^2\rangle} &= e_0 \ln N + f_0. \end{aligned} \quad (5.3)$$

The fits yield the following values:

$$\begin{aligned} c_0 &= -3.7 \cdot 10^{-3} \pm 1.7 \cdot 10^{-2} \quad , \quad d_0 = 1.117 \pm 0.076, \\ e_0 &= -1.1 \cdot 10^{-2} \pm 2.9 \cdot 10^{-2} \quad , \quad f_0 = 1.39 \pm 0.13. \end{aligned} \quad (5.4)$$

From the above values of the slopes c_0 and d_0 and the corresponding plots, we can notice a slight decrease in $\sqrt{\langle\Theta_i^2\rangle}$ when N grows. However, this change is very mild and we cannot determine that the winding angle of an intermediate atom changes when the polymer is elongated.

5.3 Winding Angle Distributions of an Ideal Polymer Between a Cone and a Plane

We now study the winding angles of an ideal polymer attached to the tip of a circular cone in the vicinity of an impenetrable plane, as depicted in Fig. 2.4(a). This configuration has no analytical solution known. Our goal is to find the dependence

of $\sqrt{\langle\Theta^2\rangle}$ on $\ln N$ for several cone opening angles α . We also find the dependence of $\sqrt{\langle\Theta_i^2\rangle}$ on $\ln N$ for $i = 10$ and $i = 20$, as done in the previous section. Simulations for this configuration are done in the same manner as described for the rod configuration, where we use $t = 2N^2$ to acquire self-contained equilibrium state and repeat this scheme 5000 times to build statistics for the problem.

Fig. 5.4 shows numerical values of $\sqrt{\langle\Theta^2\rangle}$ as a function of $\ln N$ for the last atom in the chain, for several α s. Figs. 5.5(a) and 5.5(b) show $\sqrt{\langle\Theta_{10}^2\rangle}$ and $\sqrt{\langle\Theta_{20}^2\rangle}$, respectively, as function of $\ln N$ for several α s. The results are fitted according to:

$$\begin{aligned}\sqrt{\langle\Theta^2\rangle} &= a_\alpha \ln N + b_\alpha, \\ \sqrt{\langle\Theta_{10}^2\rangle} &= c_\alpha \ln N + d_\alpha, \\ \sqrt{\langle\Theta_{20}^2\rangle} &= e_\alpha \ln N + f_\alpha.\end{aligned}\tag{5.5}$$

For clearer display, the figures only show results for some α s, where all coefficients values are shown in Table 5.1.

Fig. 5.4 shows linear dependence of $\sqrt{\langle\Theta^2\rangle}$ in $\ln N$, as seen in the rod configuration. It can be seen that the values of a_α become smaller as α increases. This means that as the cone opens, the winding angle becomes smaller for the same polymer length, which indicates that the polymer is less ‘wrapped’ around the cone. As seen for the rod configuration, by looking at the values of $\sqrt{\langle\Theta^2\rangle}$, it can be seen that the polymer actually ‘escapes’ to one side and does not surround the cone, even for large N . For large opening angles, e.g. $\alpha = 0.45\pi$, a_α is practically zero, meaning the polymer stays on the same side of the cone its starting at, and will propagate further, as seen in the previous Chapter. Surprisingly, even for small α , there is still significant difference between the winding angle in the cone-plane configuration and the rod configuration, although both cases show the same behavior as discussed above.

Fig. 5.5 shows linear behavior as expected, similar to that in Fig. 5.3. It appears that the slopes c_α and e_α are growing (in absolute value) as α increases. However, the values are very small and therefore this behavior is inconclusive. The results might imply that the winding angle of an intermediate monomer of an ideal polymer attached to a cone with large opening angle is affected by a change in the polymer length, where the effect is more noticeable as α grows. While this seems to be the trend from these plots, our results cannot give conclusive evidence for such behavior and further investigation is still needed.

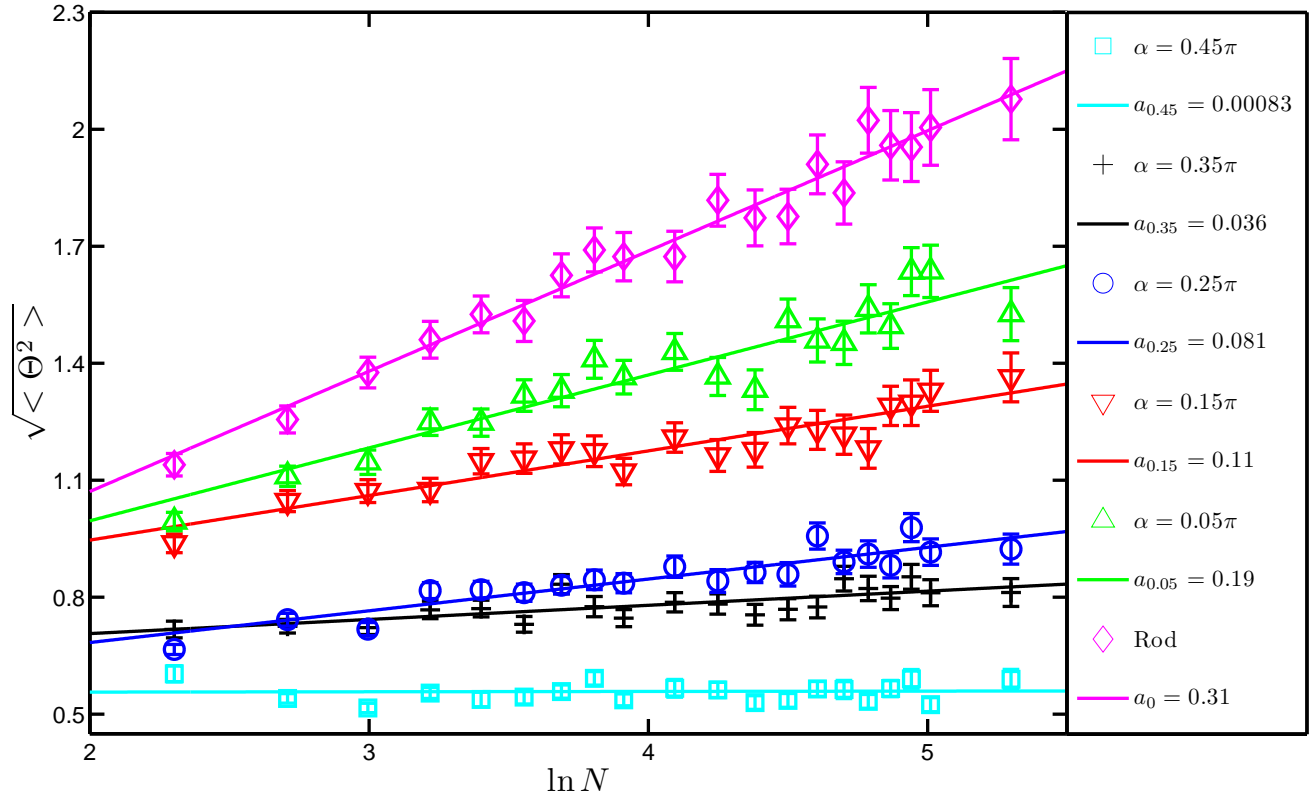
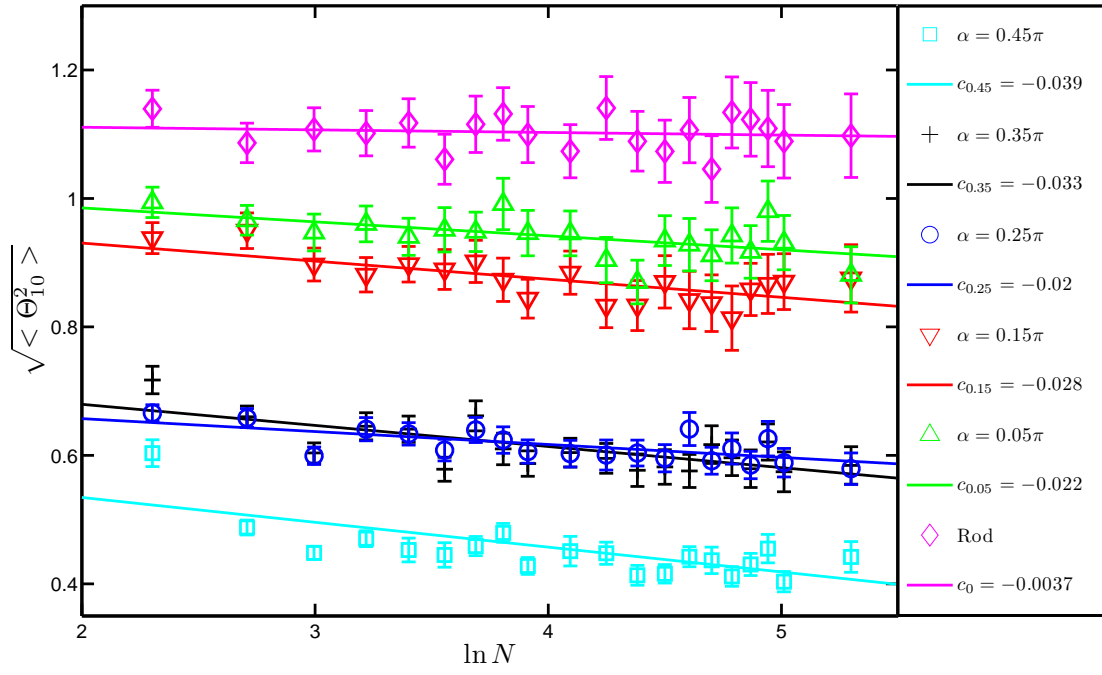
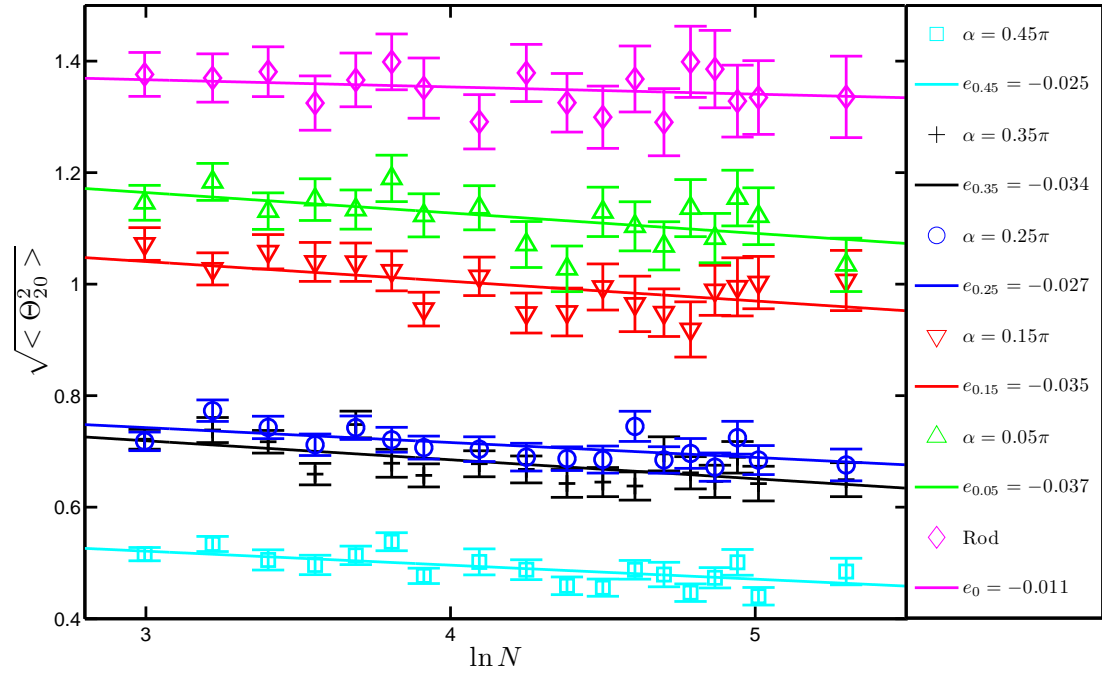


Figure 5.4: Plot of $\sqrt{\langle \Theta^2 \rangle}$ as function of $\ln N$ for an ideal polymer attached to the tip of a circular cone with opening angle α touching a plane (Fig. 2.4(a)). Numerical values are denoted by different shape and color for each α , while solid lines indicate linear fits according to (5.5). The legend on the right shows the color and shape for each set of points and its corresponding fit, as well as slope values a_α . Fits coefficients values and errors are shown in Table 5.1. All plots in this figure show linear relation between $\sqrt{\langle \Theta^2 \rangle}$ and $\ln N$, as seen for the case of an ideal polymer attached to a circular rod.



(a)



(b)

Figure 5.5: Plot of (a) $\sqrt{\langle \Theta_{10}^2 \rangle}$ and (b) $\sqrt{\langle \Theta_{20}^2 \rangle}$ as function of $\ln N$ for an ideal polymer attached to the tip of a circular cone with opening angle α touching a plane (Fig. 2.4(a)). Numerical values are denoted by different shape and color for each α , while solid lines indicate linear fits according to (5.5). The legend on the right shows the color and shape for each set of points and its corresponding fit, as well as slopes values c_α and e_α . Fits coefficients values and errors are shown in Table 5.1.

α	Last atom		10th atom		20th atom	
	a_α	b_α	c_α	d_α	e_α	f_α
0.45π	0.00083 (-0.014, 0.016)	0.55 (0.49, 0.62)	-0.039 (-0.057, -0.021)	0.61 (0.54, 0.69)	-0.025 (-0.040, 0.010)	0.59 (0.53, 0.66)
0.4π	0.012 (-0.005, 0.028)	0.63 (0.56, 0.70)	-0.037 (-0.053, -0.022)	0.69 (0.62, 0.75)	-0.041 (-0.063, -0.020)	0.77 (0.68, 0.86)
0.35π	0.036 (0.019, 0.053)	0.63 (0.56, 0.71)	-0.033 (-0.048, -0.018)	0.74 (0.68, 0.81)	-0.034 (-0.053, -0.015)	0.82 (0.74, 0.90)
0.3π	0.058 (0.026, 0.09)	0.69 (0.56, 0.83)	-0.025 (-0.049, -0.0015)	0.82 (0.72, 0.93)	-0.036 (-0.070, -0.0017)	0.96 (0.81, 1.11)
0.25π	0.081 (0.061, 0.102)	0.52 (0.43, 0.61)	-0.020 (-0.031, -0.0089)	0.69 (0.65, 0.74)	-0.027 (-0.043, -0.011)	0.82 (0.75, 0.89)
0.2π	0.081 (0.053, 0.108)	0.66 (0.54, 0.78)	-0.033 (-0.049, 0.016)	0.86 (0.79, 0.93)	-0.037 (-0.063, -0.011)	0.98 (0.87, 1.10)
0.15π	0.11 (0.091, 0.138)	0.72 (0.62, 0.82)	-0.028 (-0.043, -0.013)	0.99 (0.92, 1.05)	-0.035 (-0.061, -0.0096)	1.15 (1.03, 1.26)
0.1π	0.15 (0.13, 0.18)	0.54 (0.42, 0.67)	-0.020 (-0.038, -0.0029)	0.90 (0.82, 0.97)	-0.025 (-0.047, -0.0038)	1.08 (0.99, 1.18)
0.05π	0.19 (0.15, 0.23)	0.62 (0.46, 0.79)	-0.022 (-0.039, -0.0043)	1.03 (0.95, 1.10)	-0.037 (-0.066, -0.0073)	1.27 (1.15, 1.40)
<i>Rod</i>	0.31 (0.28, 0.34)	0.45 (0.33, 0.58)	-0.0041 (-0.020, 0.012)	1.12 (1.05, 1.19)	-0.013 (-0.039, 0.013)	1.41 (1.29, 1.52)

Table 5.1: Fit coefficients for the linear fits in Figs. 5.4 - 5.5, according to (5.5). The main number in each cell is the coefficient value, where the numbers in the parentheses show the 95% confidence interval for the coefficient. Left column shows the cone's opening angle α , where other columns show the coefficients for the last, 10th and 20th atoms, as stated in the top row.

Chapter 6

Conclusions and Future Prospects

In this work we have investigated the conformations of ideal polymers connected in one end to a scale invariant surface. We showed that in such geometries, $P(\vec{R}, N)$ can be divided into a product of a radial function and an angular function. For long polymers, i.e. $N \gg 1$, the radial function has a unique form defined by the exponent η . The first part of this work was dedicated to finding $\langle R^2 \rangle$ and η for ideal polymers in various scale-invariant geometries using lattice simulation method. In the second part, we used Monte-Carlo simulation to find the winding angle distributions of ideal polymers in a cone-plane configuration.

We started with configurations where we could find η analytically, to confirm our numerical simulations. The found numerical values of η matched the theoretical predictions excellently. Investigating configurations in which we could not find $P(\vec{R}, N)$ analytically, revealed several interesting features regarding the conformations of the polymers. We found that the more confined the polymer is, the more it stretches, as it has higher probability to end farther from the surface. This feature is due to the repulsive force between the polymer and the restricting surfaces. While this feature is not surprising, we found that it cannot be determined beforehand which surface is more ‘confining’. In general, the guideline should be that the ‘smoother’ the shape is, the less it confines the polymer propagation, leading to smaller end-to-end vector. This is of course applicable only when the two shapes are of the same scale.

In the last part of this work we looked at the winding angles of an ideal polymer around a circular cone touching a plane. We found that the linear relation between $\sqrt{\langle \Theta^2 \rangle}$ and $\ln N$ known for a polymer around a circular rod, holds for this case as well. Surprisingly, we found that the winding angles are very small, where relatively short polymers (up to $N = 200$) do not propagate around the cone. We also found no conclusive evidence for a change in the winding angle of an intermediate monomer as function of N . This part requires further investigation in order to check whether the same linear relation applies for longer polymers, i.e. larger values of N . Such numerical simulations require better computational resources and more time.

We focused entirely on the conformations of long ideal polymers in scale invariant geometries, which provides the basis for similar problems. Various extensions can be introduced to our model. The most natural extension is calculating the exponent η

for real polymers. This can be done by introducing self-avoiding walk (SAW) instead of the RW used here. While universal exponents and force amplitudes are different between ideal and real polymers models, previous studies showed similar behavior and universal exponents in both models, especially in narrow spaces. Therefore, this work may serve as a guideline for verification of results in SAW models.

Many-polymers systems such as star polymers and polymer brush can also be studied using the same methods introduced here. Such systems introduce new constraint on the single polymer, since it interacts with other polymers. These interactions should be implemented into the numerical simulations, and the end-to-end distance can be found. Geometries with length scale H , such as sphere or finite cones, satisfying the condition $\sqrt{DN} \sim H$, has been studied before [29], and can be further investigated. Such systems can be studied experimentally as well, and can help us to better understand polymer's behavior near impenetrable surfaces.

Appendix A

Simulation of Diffusing Particle on a Lattice

In this appendix we discuss the numerical method used in this work and described in Section 3.1. In this method, we solve the diffusion equation on a lattice in the vicinity of an impenetrable surface to find $P(\vec{R}, N)$.

As discussed in Section 3.1, $\eta(N)$ follows:

$$\eta(N) = a_0 + a_1 \left(\frac{1}{\sqrt{N}} \right) + a_2 \left(\frac{1}{\sqrt{N}} \right)^2 + \dots, \quad (\text{A.1})$$

where a_i s are dimensionless constants. Since we are looking at the limit of large N , we can fit $\eta(N)$ to second order in $\frac{1}{\sqrt{N}}$, so the intersection of the parabola with the y -axis is η :

$$\eta = \lim_{N \rightarrow \infty} \eta(N) = a_0. \quad (\text{A.2})$$

Since the above theorem is true only for large N , we only consider a series of the largest N s to this fit. An example can be seen in Fig. A.1, for the case of a

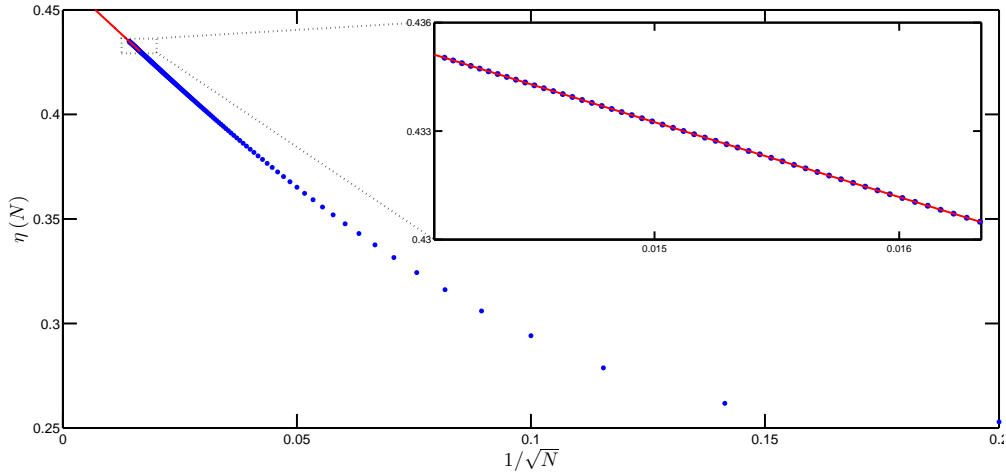


Figure A.1: Plot of $\eta(N)$ as function of $1/\sqrt{N}$ for an ideal polymer connected to the tip of a circular cone with $\alpha = \pi/4$. In this example, the simulation is done up to $N_{\max} = 5000$ with equal intervals of $\Delta N = 25$. The parabolic fit is done for $3750 \leq N \leq 5000$ (red solid line). The figure shows excellent match between the parabolic fit and the numerical points.

polymer attached to the tip of a circular cone with opening angle $\alpha = \pi/4$. The intersection point is at $a_0 = 0.4645$, where analytical value is $\eta = 0.4631$, meaning 0.3% discrepancy. By looking at the discrepancies for many geometries, we found maximum 1% discrepancy. In addition, by adding another term to the fit in (A.1), the value of η does not change more than 1%. We therefore estimate the error to be 1%, meaning:

$$\Delta\eta = 0.01\eta. \tag{A.3}$$

Another factor we must consider is the malformation in the shape due to discretization of the lattice. This malformation is most significant for polymers in narrow spaces, as depicted in Fig. A.2 for a circular cone. It can be seen that the polymer actually has ‘no place to go’ until after m steps (9 in our example), when it can then make only 1 step to each side. Assuming a free polymer can make one step to each side for each step forward, this is equivalent for the polymer in our example reaching m^2 , where he can make m steps to each side. From Fig. A.2, m satisfies:

$$m = \frac{1}{\tan(\alpha)}. \tag{A.4}$$

Therefore, the starting point of the diffuser should be:

$$r' = \frac{a}{\tan^2 \alpha}. \tag{A.5}$$

We must take this into consideration when deciding the number of steps N , since we must satisfy $\frac{r'}{a\sqrt{N}} \ll 1$. Therefore, we use larger N for narrow spaces. Note that this is only used for polymers inside cones and attached to a cone perpendicular to a plane, since this effect takes place only in these configurations.

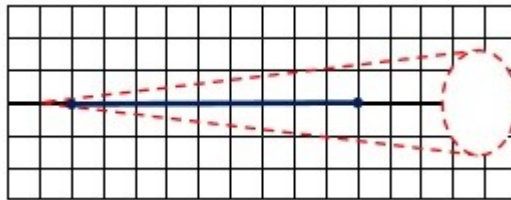


Figure A.2: A sketch demonstrating the effect of lattice discretization. Due to the cone (red dashed line), the random walker (blue solid line) cannot move to the sides until it moved 9 steps forward, where it can then make one step to each side.

Appendix B

Numerical Monte Carlo Simulation

We use Metropolis importance sampling Monte Carlo simulation [27, 28] to find the winding angle of a polymer in different geometries. The Master equation [30]

$$\frac{\partial p_n(t)}{\partial t} = - \sum_{n \neq m} [p_n(t) W_{n \rightarrow m} - p_m(t) W_{m \rightarrow n}], \quad (\text{B.1})$$

relates the probabilities $p_n(t)$ and $p_m(t)$ of the system being in states n and m at time t and the rate $W_{n \rightarrow m}$ of the transition from n to m . In equilibrium, $\partial p_n(t) / \partial t = 0$, which can be satisfied by using detailed balance:

$$p_n(t) W_{n \rightarrow m} = p_m(t) W_{m \rightarrow n}. \quad (\text{B.2})$$

In equilibrium, the probability of the n th state occurring is given by the Boltzmann distribution:

$$p_n(t) = \frac{\exp\left(-\frac{E_n}{k_B T}\right)}{Z}, \quad (\text{B.3})$$

where Z denotes the partition function, E_n the energy of the state n , k_B is the Boltzmann constant and T the temperature of the system. Any transition rate $W_{n \rightarrow m}$ satisfying equation (B.2) is acceptable, including the Metropolis form [31]:

$$W_{n \rightarrow m} = \begin{cases} \exp\left(-\frac{\Delta E}{k_B T}\right) & \Delta E > 0 \\ 1 & \Delta E < 0 \end{cases}, \quad (\text{B.4})$$

where $\Delta E \equiv E_n - E_m$.

As described earlier, we use the energy as defined in the Gaussian chain model according to equation 1.12:

$$E_n = \frac{1}{2} k \sum_{n=1}^N \left(\vec{R}_n - \vec{R}_{n-1} \right)^2,$$

with $k = \frac{2k_B T}{a^2}$. To achieve equilibrium state, we start with a possible conformation of an ideal chain. We then follow the following algorithm:

1. Choose atom i randomly.

2. Choose distance Δx from a normal distribution. Repeat the same for Δy and Δz .
3. Move the atom by $(\Delta x, \Delta y, \Delta z)$.
4. Calculate the energy change ΔE resulting from this move.
5. Generate a random number r such that $0 < r < 1$.
6. If $r < \exp(-\Delta E/k_B T)$, make the move. Else, do nothing.
7. Go back to step 1.

Note that a move to a forbidden site requires $\Delta E = \infty$, which results in 0 probability of moving to that site. The Monte Carlo (MC) time unit is defined as an attempt to move all atoms, which in our case is the number of monomers N .

The above scheme assures us that we achieve equilibrium after certain time, regardless of the initial state of the system. This time is called the *relaxation time*, and is determined experimentally. In order to find the relaxation time, we first need to find the autocorrelation function:

$$g(t) \equiv \frac{\langle A(t') A(t'+t) \rangle_{t'} - \langle A(t') \rangle_{t'}^2}{\langle A^2 \rangle - \langle A \rangle^2}, \quad (\text{B.5})$$

where $A(t)$ denotes the quantity in our interest. In our case, this quantity is Θ , and therefore we can neglect the second term since:

$$\langle \Theta \rangle = 0. \quad (\text{B.6})$$

The autocorrelation function should have the form:

$$g(t) = \sum_i C_i \exp\{-t/\tau_i\}, \quad (\text{B.7})$$

where C_i s are constants and τ_i s are relaxation times. The total relaxation time τ is calculated using:

$$\tau = \int_0^\infty g(t) dt, \quad (\text{B.8})$$

where we expect the relaxation time to be proportional to N^2 [17]. Note that the relaxation time is measured in MC time units.

An example for the autocorrelation function can be seen in Fig. B.1. The figure shows the autocorrelation function for the case of an ideal polymer attached to the tip of a circular cone with opening angle $\alpha = \pi/4$ in the vicinity of a plate, as discussed in Section 5.3. The number of monomers in this example is $N = 100$. The figure also shows fit to the first two significant terms in (B.7):

$$g(t)_{N=100} = C_1 \exp \{-t/\tau_1\} + C_2 \exp \{-t/\tau_2\}. \quad (\text{B.9})$$

From integrating the above function according to (B.8), we find the relaxation time to be $\tau = 26.9N^2$. Calculations of the relaxation time for other values of N show similar results as expected, with pre-factor smaller than 30 for all N . Due to computational limitations, we choose to document the locations of the monomers every

$$t_0 = 2N^2. \quad (\text{B.10})$$

For numerical purposes, this means that the scheme described in Section 5.1 should

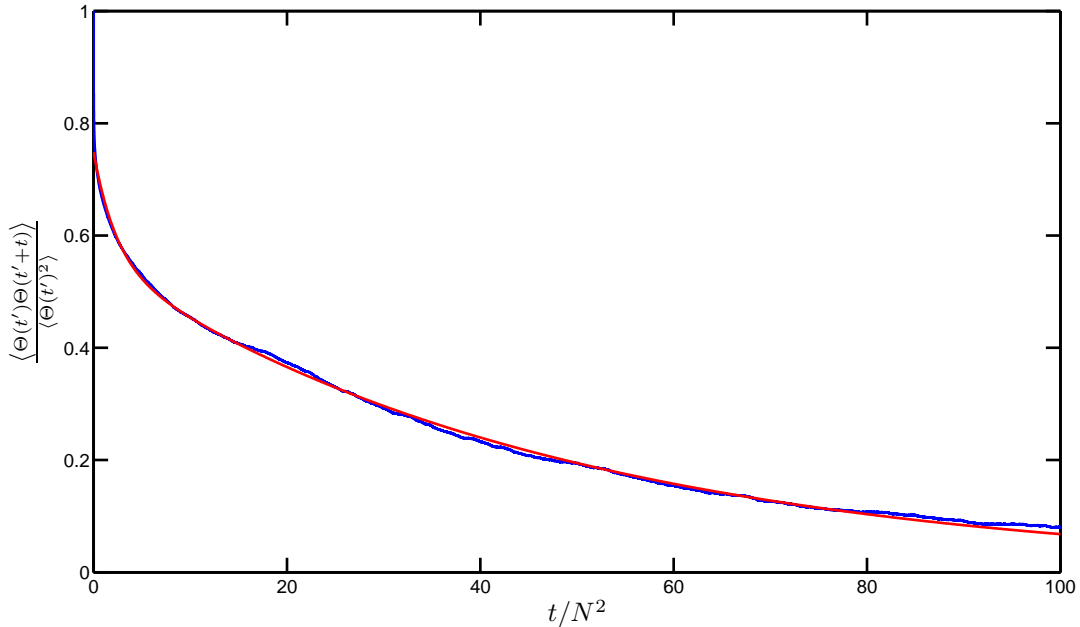


Figure B.1: The normalized autocorrelation function $g(t) \equiv \frac{\langle \Theta(t')\Theta(t'+t) \rangle_{t'}}$ (blue line) as a function of t for an ideal polymer with $N = 100$ attached to the tip of a circular cone with opening angle $\alpha = \pi/4$ near a plane. Note that the x -axis is in MC time units, where each time unit is N . Red line indicates fit to the numerical values according to equation (B.9). The relaxation time here is found to be $\tau = 26.9N^2$.

repeat itself $2N^3$ times in order to acquire a single polymer conformation in equilibrium state. To build statistics for the problem, we took the winding angle of each monomer for $T = 5000$ different conformations, for each configuration. Since the relaxation time is larger than what we have chosen by factor ~ 15 , only $T/15$ conformations are uncorrelated. We use this measure in our error calculations.

The errors for this method are calculated according to:

$$\Delta \left(\sqrt{\langle \Theta^2 \rangle} \right) = \frac{\Delta \langle \Theta^2 \rangle}{2\sqrt{\langle \Theta^2 \rangle}}, \quad (\text{B.11})$$

where the standard deviation of $\langle \Theta^2 \rangle$ is:

$$\Delta \langle \Theta^2 \rangle = \sqrt{\langle \Theta^4 \rangle - \langle \Theta^2 \rangle^2}. \quad (\text{B.12})$$

As discussed above, only $\frac{T}{15}$ conformations are considered uncorrelated. Therefore, we need to insert the factor $\frac{T}{15}$ into the error. We thus estimate the error to be:

$$\Delta \left(\sqrt{\langle \Theta^2 \rangle} \right) = \frac{\sqrt{\langle \Theta^4 \rangle - \langle \Theta^2 \rangle^2}}{2\sqrt{\langle \Theta^2 \rangle} \frac{T}{15}}. \quad (\text{B.13})$$

We use this error for all the plots in Chapter 5.

References

- [1] C. Bustamante, J.C. Macosko and G.J.L. Wuite, *Nature Reviews Molecular Cell Biology*, **1**, 130–136 (2000).
- [2] M.S.Z. Kellermayer, *Physiological Measurement*, **26**, R119 (2005).
- [3] K.C. Neuman, T. Lionnet and J.F. Allemand, *Annual Review of Materials Research*, **37**, 33–67 (2007).
- [4] D. Sarid, *Scanning Force Microscopy* (Oxford University Press, New York, 1994).
- [5] F.J. Giessibl, *Reviews of Modern Physics*, **75**, 949 (2003).
- [6] T.H. Nguyen *et al.*, *Nanotechnology*, **21**, 075101 (2010).
- [7] A. Kishino and T. Yanagida, *Nature*, **334**, 74–76 (1988).
- [8] J.R. Moffitt *et al.*, *Annual Review of Biochemistry*, **77**, 205–228 (2008).
- [9] C. Gosse and V. Croquette, *Biophysical Journal*, **82**, 3314–3329 (2002).
- [10] I. de Vlaminck and C. Dekker, *Annual Review of Biophysics*, **41**, 453–472 (2012).
- [11] R. Rubinstein and R.H. Colby, *Polymer Physics* (Oxford University Press, New York, 2003).
- [12] P.G. de Gennes, *Scaling Concepts in Polymer Physics* (Cornell University Press, Ithaca, 1979).
- [13] M. Doi, *Introduction to Polymer Physics* (Oxford University Press, New York, 1992).
- [14] S. Chandrasekhar, *Reviews of Modern Physics*, **15**, 1–89 (1943).
- [15] F. Spitzer, *Principles of Random Walk* (Springer Verlag, New York, 2001).
- [16] B.D. Hughes, *Random Walks and Random Environments: Volume 1: Random Walks* (Oxford University Press, New York, 1995).
- [17] M. Doi and S.F. Edwards, *The Theory of Polymer Dynamics* (Oxford University Press, New York, 1988).

- [18] H.S. Carslaw and J.C. Jaeger, *Conduction of Heat in Solids* (Oxford University Press, Oxford, 1959).
- [19] S. Rosenberg, *The Laplacian on a Riemannian Manifold: An Introduction to Analysis on Manifolds* (Cambridge University Press, Cambridge, 1997).
- [20] E. Ben-Naim and P.L. Krapivsky, *Journal of Physics A: Mathematical and Theoretical*, **43**, 495007 (2010).
- [21] M.F. Maghrebi, Y. Kantor and M. Kardar, *Physical Review E*, **86**, 061801 (2012).
- [22] J. Rudnick and Y. Hu, *Journal of Physics A: Mathematical and General*, **20**, 4421–4438 (1987).
- [23] B. Drossel and M. Kardar, *Physical Review E*, **53**, 5861 (1996).
- [24] H. Saleur, arXiv:hep-th/9310034, (1993).
- [25] D. Considine and S. Redner, *Journal of Physics A: Mathematical and General*, **22**, 1621 (1989).
- [26] M. Abramowitz and I.A. Stegun, *Handbook of Mathematical Functions: With Formulas, Graphs, and Mathematical Tables* (US Government Printing Office, Washington DC, 1972).
- [27] K. Binder and D.W. Heermann, *Monte Carlo Simulation in Statistical Physics: An Introduction* (Springer Verlag, Berlin, 2010).
- [28] D.P. Landau and K. Binder, *A Guide to Monte Carlo Simulations in Statistical Physics* (Cambridge University Press, 2005).
- [29] R. Bubis, Y. Kantor and M. Kardar, *Europhysics Letters*, **88**, 48001 (2009).
- [30] F. Reif, *Fundamentals of Statistical and Thermal Physics* (McGraw-Hill, New York, 1965).
- [31] N. Metropolis *et al.*, *The Journal of Chemical Physics*, **21**, 1087 (1953).

TEL AVIV UNIVERSITY
Raymond and Beverly Sackler
Faculty of Exact Sciences
School of Physics & Astronomy



אוניברסיטת תל-אביב

הפקולטה למדעים מדויקים
ע"ש ריימונד וברלי סאקלר
בית הספר לפיסיקה ואסטרונומיה

קונפורמציות של פולימרים במרחבים מוגבלים

חיבור זה הוגש כחלק מהדרישות לקבלת התואר
"מוסמך אוניברסיטה" (M.Sc.) בפיסיקה באוניברסיטת תל-אביב
בית הספר לפיסיקה ואסטרונומיה

על-ידי

ניר אלפסי

עבודת מחקר זו בוצעה תחת הנחייתו
של פרופסור יעקב קנטור

אוגוסט 2013

תקציר

ההתקדמות האחרונה בשיטות מניפולציה של מולקולות בודדות מאפשרת לנו למדוד כוחות מסדר גודל של pN. לרוב בשיטות אלו, פולימר מחובר מצדו האחד לקצהו של גשוש (probe) מיקרוסקופי המתקרב למשטח. בשלב זה, נמדד הכוח המופעל על המשטח על ידי הפולימר ביחס למרחקו מהמשטח. בעבודה זו, אנו חוקרים כוחות אלו. במודל שעליו אנו מסתכלים, הכוח הוא ממקור אנטרופי בלבד, עם משרעת A הנקבעת על ידי הפרש בין האקספוננט האוניברסלי η של שתי גיאומטריות חסרות סקאלה שונות.

אנו מוצאים את הקונפורמציות של פולימרים אידאליים בגיאומטריות אלו, ומסיקים מתוכן את המרחק קצה-קצה של הפולימר, אשר קשור לאקספוננט η . אנו מבצעים סימולציות על סריג היפר-קובי על מנת למצוא את η במספר גיאומטריות חסרות סקאלה, כגון קונוס עם חתכים שונים, שני קונוסים מעגליים וקונוס מעגלי הנוגע במשטח. אנו מסתכלים על הגבול של פולימרים ארוכים בלבד, כאשר המשטחים נחשבים לאינסופיים.

תוצאות הסימולציות שלנו תואמות בצורה מושלמת את התחזיות האנליטיות. אנו חוקרים בנוסף גיאומטריות רבות שלא ניתן למצוא להן פתרון אנליטי. אנו מוצאים שככל שהפולימר מוגבל יותר, כך המרחק קצה-קצה גדול יותר. בנוסף, אנו מראים שכאשר הפולימר מוגבל יותר באיזור מסויים במרחב, הוא 'בורח' לאיזור הפתוח יותר ותכונותיו משתנות בהתאם.

אנו חוקרים בנוסף את זווית הליפוף (winding angle) של פולימר המחובר בקצהו לקונוס בצמוד למשטח. אנו מראים שפולימרים קצרים יחסית אינם מקיפים את הקונוס, אלא 'בורחים' לצד אחד של הקונוס ומתפשטים שם. אנו חוקרים גם את זווית הליפוף של מונומרים במרכז השרשרת הפולימרית, ולא מוצאים ראיות ממשיות לכך שזווית הליפוף שלהם משתנה כאשר הפולימר מוארך.